Distribution Category:
LMFBR Safety--Base
Technology (UC-79p)

ANL-82-77

ANL--82-77

DE83 004399

ARGONNE NATIONAL LABORATORY
9700 South Cass Avenue
Argonne, Illinois 60439

DYNAPCON: A COMPUTER CODE FOR DYNAMIC ANALYSIS OF PRESTRESSED CONCRETE STRUCTURES

by

A. H. Marchertas

Reactor Analysis and Safety Division

September 1982

TABLE OF CONTENTS

LIST OF FIGURES

LIST OF TABLES

DYNAPCON A COMPUTER CODE FOR DYNAMIC ANALYSIS OF PRESTRESSED CONCRETE STRUCTURES

by

A. H. Marchertas

ABSTRACT

A finite element computer code for the transient analysis of prestressed concrete reactor vessels (PCRVs) for LMFBR containment is described. The method assumes rotational symmetry of the structure. Time integration is by an explicit method. The quasi-static prestressing operation of the PCRV model is performed by a dynamic relaxation technique. The material model accounts for the crushing and tensile cracking in arbitrary direction in concrete and the elastic-plastic behavior of reinforcing steel. The variation of the concrete tensile cracking and compressive crushing limits with strain rate is taken into account. Relative slip is permitted between the concrete and tendons.

Several example solutions are presented and compared with experimental results. These sample problems range from simply supported beams to small scale models of PCRV's. It is shown that the analytical methods correlate quite well with experimental results, although in the vicinity of the failure load the response of the models tend to be quite sensitive to input parameters.

I. INTRODUCTION

The analysis of reinforced concrete has been the topic of many investigations, beginning with the original work of Nilson [1] who duplicated the cracking pattern in a point loaded, simply supported beam. Recently, a definitive paper describing the use of a Mohr-Coulomb model was published by Argyris, et al. [2], which demonstrated the application of a finite element procedure to a large variety of static problems.

The analysis of prestressed concrete under impulsive loads such as in the safety analysis of a hypothetical core disruptive accident (HCDA), however, poses additional difficulties. An efficient solution under such conditions makes an explicit technique preferable, both because of economy and because it facilitates the use of a realistic model of the interaction of prestressing tendons with the concrete through the slide line option; the latter are very difficult to program in implicit, Newton type codes. However, this necessitates an efficient solution procedure for the static prestressing. Dynamic relaxation procedures provide a natural method for obtaining static solutions by explicit, transient codes, and finite difference procedures for its implementation have been published by Otter [3], and Holland [4] and the group at Imperial College [5]. However, little was available for enhancing the efficiency of dynamic relaxation in a finite element context, so we have developed such procedures, and describe them in Section III.A.

Another difficulty which has plagued our treatment of concrete models with cracking in a dynamic setting is the chain reaction of cracks introduced by cracking in a single element [6,7]. This often leads to complete failure of the structure in situations where experiments do not indicate failure. One of the culprits in our initial models was the complete elimination of tensile normal stress across the crack immediately after cracking. We have now refined this model by introducing a gradual decay in tensile stress and found experimental evidence for this phenomenon in the literature [8]. In addition we have incorporated the strain rate dependence of the tensile strength of concrete. The incorporation of these factors has led to reasonable agreement between our model and many experiments; some of these comparisons are reported here.

II. BASIC FEATURES OF THE ANALYTICAL METHOD

In view of the significant advantages of the finite-element technique for engineering analysis, it was adopted for these models. Rather than developing a completely new code, the WHAMS [9] code is used as a basis. One feature which sets this family of codes apart from other codes is its use of convected coordinates. In the use of convected coordinates, each element is associated with a coordinate system that rotates but does not deform with the element. For problems with small strains but large rotations, which probably encompasses a large portion of nonlinear engineering problems, it can be shown that the strains are linearly related to what are termed "deformation displacements". The latter are simply the displacements of the element relative to the convected coordinates. The deformation nodal forces are similarly related to the stresses by linear expressions. The important nonlinearities which arise from large rotations are accounted for entirely by transformations between the global and convected coordinates and the omission of the rigid body motion in the strain-displacement relations. Hence, the computation of nodal forces is considerably simplified, particularly in elements where numerical quadrature is required.

For treating prestressed concrete structures, this parent code has been supplemented by a material law that models cracking and reinforcement distributed within a continuum finite element. In programs with explicit time integration, the material properties are used exclusively to calculate stress increments from strain increments, and the implementation of constitutive equations must be arranged accordingly.

Three basic components are needed for modeling reinforced and prestressed concrete structures. These are:

- a means of representing concrete behavior under an applied load,
- a method of accounting for the contribution of concrete reinforcement,
- the provision for a prestressing capability.

The first two items, concrete and reinforcement, are modeled by a homogination approach, so that the stresses of both concrete and steel are averaged to obtain the element stress. Thus, the formulation provides the equivalent components of stress (σ_{rr}, σ_{zz}, σ_{rz}, $\sigma_{\theta\theta}$) from a known state of strain (ε_{rr}, ε_{zz}, γ_{rz}, $\varepsilon_{\theta\theta}$). A total stress-strain formulation, as opposed to an incremental one, is used. The prestressing capability is handled outside of the reinforced concrete formulation. This is accomplished by the use of separate elements representing prestressing tendons. A detailed description of the analytical models is provided in the following paragraphs.

A. Time Integration

Time integration is carried out by the central difference explicit method. For the central-difference method, the velocities and displacements are updated by the formulas

$$\dot{\underline{u}}(t + \Delta t/2) = \dot{\underline{u}}(t - \Delta t/2) + \Delta t\ \ddot{\underline{u}}(t) \tag{1}$$

and

$$\underline{u}(t + \Delta t) = \underline{u}(t) + \Delta t\ \dot{\underline{u}}(t + \Delta t/2)\ , \tag{2}$$

where superscript dots denote time derivatives and Δt is the time step. For purposes of numerical stability the time step is limited by

$$\Delta t < \frac{2}{\omega_{max}} \left(\sqrt{1 + \mu^2} - \mu\right)\ , \tag{3}$$

where ω_{max} is the maximum frequency in the mesh, and μ is the fraction of critical damping in the highest frequency due to the stiffness proportional damping; μ is independent of any mass-proportional (diagonal) damping.

To estimate Δt for a run, we use the result of Hughes, et al. [10] that the maximum frequency of the mesh is bounded by the maximum frequency of any individual element in the mesh. For constant-strain elements the highest frequency may be estimated by the formula

$$\omega_{max} = \frac{2c}{\ell}\ , \tag{4}$$

where c is the maximum elastic or the acoustic-wave speed in the material and ℓ the minimum element dimension. This estimate also applies to the axial mode of the beam and shell elements, but in addition a bending mode must be considered for which the frequency estimate is

$$\omega_{max} = \frac{12cr_g}{\ell^2}\ , \tag{5}$$

where r_g is the radius of gyration of the cross section. For a uniform cross section, the radius of gyration is given by $r_g^2 = h^2/12$, where h is the thickness. Since both Eqs. (4) and (5) pertain to a beam or shell, the time step is governed by whichever of these frequencies is larger. Thus Eq. (4) governs for a beam or shell of uniform cross-section as long as

$$\ell > \sqrt{3}h \quad (6)$$

It is important to keep the beam or shell elements long enough so that Eq. (6) is not violated by much, for otherwise Eq. (5) governs and Δt decreases with the square of element length.

The dilatational elastic wave speed c is given by

$$\left.\begin{aligned} c &= \sqrt{\frac{E}{\rho}} && \text{for beam and shell element} \\ c &= \sqrt{\frac{E}{\rho(1-\nu^2)}} && \text{for plane stress continuum} \\ c &= \sqrt{\frac{E(1-\nu)}{\rho(1-2\nu)(1+\nu)}} && \text{for plane strain continuum or axisymmetric element} \end{aligned}\right\} \quad (7)$$

where E is Young's modulus, ν is Poisson's ratio, and ρ the density.

B. Elements

Two elements have been used for the analysis of reinforced/prestressed concrete structures: a linear displacement, triangular, toroidal (or plane) continuum element and a conical shell (or beam) element. Both elements have been programmed so that they automatically reduce from axisymmetric to plain geometry. Consequently, only the axisymmetric elements will be described here. These elements are shown in Fig. 1 along with the nomenclature used in this report.

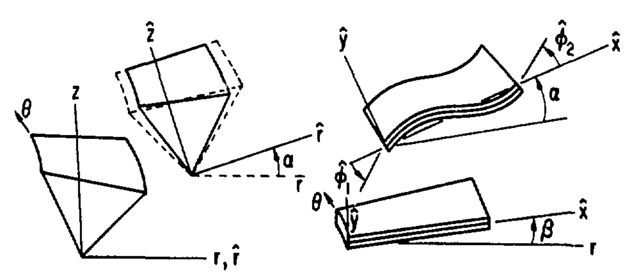

Fig. 1. The Axisymmetric Three Dimensional Continuum Element and the Axisymmetric Shell Element.

The triangular element is the standard simplex element; its displacement field relative to node 1 is given by

$$\begin{Bmatrix} u_r \\ u_z \end{Bmatrix} = \begin{bmatrix} a_1 & a_2 \\ a_3 & a_4 \end{bmatrix} \begin{Bmatrix} \hat{r} \\ \hat{z} \end{Bmatrix} . \quad (8)$$

The angle of rigid body rotation α is constant in the element and computed by the formula:

$$\tan \alpha = \frac{a_3 - a_2}{2 + a_1 + a_4} = \frac{\hat{z}_3 D_{z2} - \hat{z}_2 D_{z3} + \hat{r}_3 D_{r2} - \hat{r}_2 D_{r3}}{4A + \hat{z}_3 D_{r2} - \hat{z}_2 D_{r3} - \hat{r}_3 D_{z2} + \hat{r}_2 D_{z3}} , \quad (9)$$

where A is the area of the element, $(\hat{r}_i, \hat{z}_i)$ the nodal coordinates relative to node 1, and (D_{ri}, D_{zi}) the nodal displacements relative to the displacement of node 1. The deformation nodal displacements are found at each node by subtracting the nodal displacements which correspond to the rigid body rotation α, yielding

$$\begin{Bmatrix} \hat{D}_{ri} \\ \hat{D}_{zi} \end{Bmatrix}^{def} = [\lambda] \begin{Bmatrix} D_{ri} \\ D_{zi} \end{Bmatrix} + ([\lambda] - [I]) \begin{Bmatrix} r_i \\ z_i \end{Bmatrix} , \quad (10)$$

where

$$[\lambda] = \begin{bmatrix} \cos \alpha & \sin \alpha \\ -\sin \alpha & \cos \alpha \end{bmatrix} . \quad (11)$$

The convected strains are then given in terms of the deformation displacements by

$$
\begin{Bmatrix} \hat{\varepsilon}_r \\ \hat{\varepsilon}_z \\ \hat{\gamma}_{rz} \end{Bmatrix} = \begin{bmatrix} \partial/\partial\hat{r} & 0 \\ 0 & \partial/\partial\hat{z} \\ \partial/\partial\hat{z} & \partial/\partial\hat{r} \end{bmatrix} \begin{Bmatrix} \hat{u}_r^{def} \\ \hat{u}_z^{def} \end{Bmatrix} . \tag{12}
$$

Since the rigid body motion has been eliminated in obtaining the deformation displacements, as long as the strains are small, the above formulas are applicable regardless of the magnitude of the rotations.

Using Eq. (12), it follows that the r-z strains in the convected coordinates are then related to the deformation nodal displacements by

$$
\begin{Bmatrix} \hat{\varepsilon}_r \\ \hat{\varepsilon}_z \\ \hat{\gamma}_{rz} \end{Bmatrix} = \frac{1}{2A} \begin{bmatrix} \hat{z}_3 & 0 & -\hat{z}_2 & 0 \\ 0 & -\hat{r}_3 & 0 & \hat{r}_2 \\ -\hat{r}_3 & \hat{z}_3 & \hat{r}_2 & -\hat{r}_2 \end{bmatrix} \begin{Bmatrix} \hat{D}_{r2} \\ \hat{D}_{z2} \\ \hat{D}_{r3} \\ \hat{D}_{z3} \end{Bmatrix}^{def} . \tag{13}
$$

The circumferential strains are computed by the linear relation

$$
\varepsilon_\theta = u_r/r . \tag{14}
$$

Stresses and strains are measured in the convected coordinates, so they are independent of the rotation.

We define internal nodal forces due to planar and circumferential stresses by

$$
(f^P)_I = [T]^T \int_{V_I} [E^P]^T \{\hat{\sigma}\} dV , \tag{15}
$$

$$(f^c)_I = \int_{V_I} [E^c]^T \{\sigma_\theta\} dV \ . \tag{16}$$

The nodal forces $(f^p)_I$ are self-equilibrated.

The $[E^p]$ matrix is defined by Eq. (13), while the standard relation between ε_θ and u_r defines the $[E^c]$ matrix. The nodal forces can then be found by a direct application of Eq. (15), which yields

$$\begin{Bmatrix} f^p_{2x} \\ f^p_{2y} \\ f^p_{3x} \\ f^p_{3y} \end{Bmatrix} = \begin{bmatrix} [\lambda]^T & [0] \\ [0] & [\lambda]^T \end{bmatrix} \int_{V_I} [E^p]^T \{\hat{\sigma}\} dV \ , \tag{17}$$

$$\begin{aligned} f^p_{1x} &= -(f^p_{2x} + f^p_{3y}) \ , \\ f^p_{1y} &= -(f^p_{2y} + f^p_{3y}) \ . \end{aligned} \tag{18}$$

The integrands in Eq. (17) are not constant, but a one point integration has been found sufficient.

In the conical shell element the convected $\hat{x}$ axis is taken to lie along the line joining the nodes. Cubic polynomial shape functions in $\hat{x}$ are used for the transverse displacements, linear shape functions for the axial displacements. The rotation is not constant within this type of element, but since the strains are assumed to be small, the rotation relative to the $\hat{x}$ axis should also be small, and hence the rotation of the $\hat{x}$ axis, α, should be a good approximation of the rotational component of the element's displacement.

The deformation displacements are then the nodal rotations relative to the $\hat{x}$ axis

$$\hat{\phi}_i = \phi_i - \alpha \ , \tag{19}$$

and the midplane displacement, which can immediately be expressed in terms of the midplane strain $\hat{\varepsilon}_m$.

The strain-displacement equations are

$$\hat{\varepsilon}_x = \hat{\varepsilon}_m - \hat{y} \frac{\partial \hat{\phi}(\hat{x})}{\partial \hat{x}} , \tag{20}$$

$$\varepsilon_\theta = \frac{1}{r} \left(u_r - \hat{y} \cos \beta \frac{\partial u_y}{\partial \hat{x}}\right) , \tag{21}$$

where

$$\hat{\varepsilon}_m \overset{def}{=} \frac{\partial \hat{u}_x}{\partial \hat{x}} , \tag{22}$$

and for the transverse cubic displacement field

$$\hat{\phi}(x) = \frac{\hat{\phi}_1}{\ell^2} \left(\ell^2 - 4\ell\hat{x} + 3\hat{x}^2\right) + \frac{\hat{\phi}_2}{\ell^2} \left(3\hat{x}^2 - 2\ell\hat{x}\right) . \tag{23}$$

Equation (21) is the standard equation for the circumferential strains as given by Novozhilov [11], whereas Eq. (20) can be shown to be equivalent to that of Novozhilov within second order terms in $\hat{\varepsilon}_m$ and $\partial\hat{\phi}/\partial\hat{x}$; both terms are small for moderate rotations if the strains are small.

The stresses are then computed by the usual engineering stress-strain laws. The equations for internal nodal forces corresponding to Eq. (15) are

$$\begin{Bmatrix} m_1^p \\ m_2^p \\ \hat{f}_{2x}^p \end{Bmatrix} = -\frac{1}{\ell^2} \int_{V_I} \begin{bmatrix} (6\hat{x} - 2\ell)\hat{y} \\ (6\hat{x} - 2\ell)\hat{y} \\ \ell \end{bmatrix} \hat{\sigma}_x dV . \tag{24}$$

The other nodal forces are found by invoking the self-equilibration of the planar nodal forces

$$\hat{f}^p_{1y} = -\hat{f}^p_{2y} - (m^p_1 + m^p_2)/\ell ,$$

(25)

$$\hat{f}^p_{1x} = \hat{f}^p_{2x} .$$

These nodal forces are then transformed into the global coordinates. The internal nodal forces due to the circumferential stresses are computed by the standard linear nodal force-stress relations.

For both elements, lumped masses are used. In the axisymmetric triangular element, the total mass is apportioned equally among the three nodes. In the conical shell element, the translatory and rotatory lumped mass at each node is equivalent to the mass and mass moment, respectively, of the segment between the node and the midpoint of the element. Inertia due to rotation of the cross-section is neglected.

III. SIMULATION OF PRESTRESSING

Prestressing is an essential part of the PCRV behavior; therefore, in the analytical model, the prestress must be simulated before the dynamic loads are applied. In this prestressing simulation cracking is not permitted; here the loading is of a static nature, as opposed to the dynamic loading for which the code is primarily intended. Dynamic relaxation, described in Section III.A, is used in this phase of the modeling.

The prestressing is accomplished by layers of homogeneously distributed tendons which are modeled by thin membrane elements in the plane geometry and by thin shell elements (with $\nu = G = 0$ in the plane of the shell) in the axisymmetric geometry. These prestressing members are superimposed over the grid of the reinforced concrete model and are connected through sliding interfaces so that they can stretch and slide along a predetermined path, simulating the behavior of the tendons.

The tendons are prestressed by gradually applying a force at the points where the tendons are attached to the concrete. An equal and opposite force is also exerted on the concrete grid at these nodes so that equilibrium is maintained. When the specified prestress is reached, the prestressing tendons and concrete are locked together at these nodes. The prestressing operation is then considered complete.

A. Dynamic Relaxation

Dynamic relaxation is a procedure for obtaining static solutions by solving the dynamic equations with sufficient damping to converge to the static solution. Damping may be either diagonal damping $\underline{C}\,\dot{\underline{u}}$, where $\underline{C}$ is a diagonal matrix usually taken to be proportional to the mass matrix, or the non-diagonal damping, such as stiffness proportional damping $\alpha_1\,\underline{K}\,\underline{u}$. The equations of motion are then

$$\underline{M}\,\ddot{\underline{u}} + (\underline{C} + \alpha_1\,\underline{K})\,\dot{\underline{u}} + \underline{K}\,\underline{u} = \underline{F}^{ext} , \tag{26}$$

where $\underline{M}$, $\underline{K}$ and $\underline{C}$ are the mass, stiffness and damping matrices, $\underline{F}^{ext}$ the external force matrix, and $\underline{u}$ the nodal displacement matrix; superposed dots denote time derivatives.

In nonlinear problems $\underline{K}\,\underline{u}$ is replaced by nodal internal forces $\underline{F}^{int}$. Furthermore, the diagonal damping matrix $\underline{C}$ is taken to be mass-proportional, so $\underline{C} = \alpha_2\,\underline{M}$. Consequently, Eq. (26) can be rearranged as follows:

$$\underline{M}\,\ddot{\underline{u}} = \underline{F}^{ext} - \underline{F}^{int} - \underline{F}^{visc} , \tag{27}$$

where

$$\underline{F}^{visc} = (\alpha_1\,\underline{K} + \alpha_2\,\underline{M})\,\dot{\underline{u}} . \tag{28}$$

In order to take advantage of an implicit formulation for the mass-proportional damping terms, we use the following difference form of Eq. (27):

$$\underline{M}\ddot{u}(t) = \underline{F}^{ext}(t) - \underline{F}^{int}(t) - \alpha_1\,\underline{K}\,\dot{\underline{u}}(t - \Delta t/2) - \alpha_2\,\underline{M}\,\dot{u}(t) , \tag{29}$$

where

$$\dot{u}(t) = \frac{1}{2\Delta t}\,[u(t + \Delta t) - u(t - \Delta t)] = \dot{u}(t - \Delta t/2) + \frac{\Delta t}{2}\,\ddot{u}(t) . \tag{30}$$

Hence,

$$\underline{M}(1 + \alpha_2 \Delta t/2)\ddot{u}(t) = \underline{F}^{ext}(t) - \underline{F}^{int}(t) - (\alpha_1 \underline{K} + \alpha_2 \underline{M})\dot{u}(t - \Delta t/2) \ , \qquad (31)$$

can be used to solve for the accelerations at time t. The velocities and displacements are then obtained by Eqs. (1) and (2).

To estimate the parameters α_1 and α_2, it is necessary to have estimates on the minimum and maximum frequencies of the mesh, ω_{min} and ω_{max}. If we set $\alpha_1 = 2\beta_1/\omega_{max}$, $\alpha_2 = 2\beta_2\omega_{min}$, where β_i is the fraction of critical damping desired in the frequencies ω_i. If $\beta = \beta_1 = \beta_2$, all frequencies between ω_{min} and ω_{max} will be damped at fractions of critical damping that are less than β.

The density plays a purely fictitious role in dynamic relaxation. Whenever the elements vary in size significantly, convergence can be enhanced if ω_{max}^{ele} is the same for all elements. This is accomplished by choosing the density for each continuum element such that

$$\rho^{ele} = \frac{\omega_{max}^2 \ E(1 - \nu)}{4\ell^2(1 + \nu)(1 - 2\nu)} \ , \qquad (32)$$

where ω_{max} can be any convenient constant, which will correspond roughly with the maximum frequency of the resulting model. Similar scaling formulas are available for the shell element.

B. Sliding Interface

The movement of prestressing tendons with respect to the reinforced concrete continuum is implemented by a sliding option. The node structure at a sliding interface as used herein is shown in Fig. 2. At each point of the interface we have two nodes: one node which

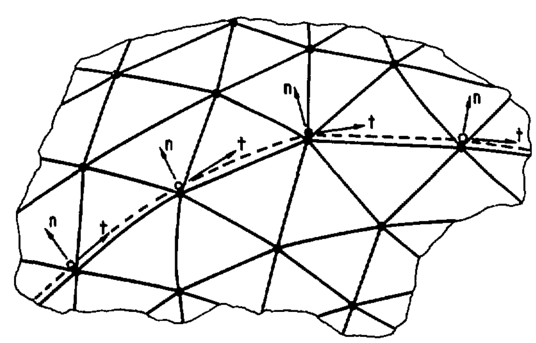

Fig. 2. Nodes of the Sliding Interface.

pertains to the prestressing tendon, and one node of the concrete grid. Initially the pairs are coincident. For each pair, a local coordinate system (t, n) is set up so that t is the tangent to the sliding interface, n is 90° counterclockwise from t. Whenever a corner occurs in the interface, t is the average of the two tangent directions.

The normal force transmitted from node i to node j across the interface is

$$f_n = F_{ni}^{int} - M_i \ddot{u}_n , \tag{33}$$

where

$$\ddot{u}_n = \frac{F_{ni} + F_{nj}}{M_i + M_j} . \tag{34}$$

Here $\ddot{u}_n$ is the common normal acceleration of the pair of nodes and the last term in Eq. (33) is the inertial resistance of node i.

IV. REINFORCED CONCRETE MODEL

Both concrete and reinforcement are modeled within the same continuum element. The strength of concrete and reinforcement are accounted for by addition of their respective stresses and resolution of resulting internal forces to the appropriate nodes. The individual models of concrete and reinforcement are described in the following sections.

A. Concrete Modeling

A linear elastic response with tensile and compressive limits is used for modeling concrete behavior. In compression, the concrete model is allowed to sustain stresses up to the uniaxial compressive strength f_c'. In tension, cracking is assumed to initiate when the maximum principal tensile stress of concrete reaches the uniaxial tensile limit f_t'.

The tensile and compressive limits of concrete are greatly dependent on the rate of loading. Some experimental evidence on this subject has been compiled by Neville [12], who plotted data showing the dependence of ultimate stress on the stress rate as obtained from McHenry and Shideler [13] and McNeeley and Lash [14]. To make use of these data in the analytical treatment of concrete, we have expressed rate dependence in terms of strain rate by using $\dot{\sigma} = E_0 \dot{\varepsilon}$, where E_0 is the initial yield modulus, and $\dot{\sigma}$ and $\dot{\varepsilon}$ are the stress and strain rates, respectively. Thus we neglect any strain rate effects on Young's modulus. The replotted ratio of dynamic strength to static strength as a function of strain rate $\dot{\varepsilon}$ is shown in Fig. 3. The static strength in Fig. 3 is assumed to be that obtained at 12 MPa/min, and $E_0 = 2.76 \times 10^4$ MPa. As observed in Fig. 3, the compressive data extend to almost 10 s^{-1}; no information for transient tensile limits is available for such strain rates.

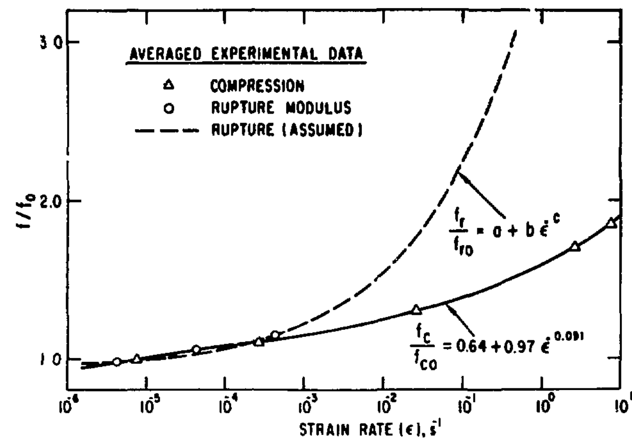

Fig. 3. Strain Rate Dependence on Tensile and Compressive Limits.

In the problems solved here, strain rates as high as 100 s^{-1} were encountered. An extrapolation of dynamic stress limit under tensile loading is thus needed. This was accomplished in the following manner.

We assume that ratio f/f_0 to be a function of strain rate $\dot{\varepsilon}$ of the exponential form*

$$\frac{f}{f_0} = a + b(\dot{\varepsilon})^c \ , \tag{35}$$

where a, b and c are constants to be determined. Two conditions could be satisfied by the experimental data shown in Fig. 3, and the third could be

---

* It is of interest to observe that a similar exponential strain rate dependence for oil shale, based on experimental data, has also been reported recently by Grady and Kipp [15].

derived by trial and error, using the analytical model described below. As the criterion for the analytical cracking, we assume that cracking is only possible as a result of structural deformation. Implied in this is the assumption that cracking will not be caused by sharp stress peaks during wave interactions.

Figure 3 also shows the equation derived for predicting dynamic compression limits. The ratio of actual strength to static strength in compression thus becomes

$$f_c/f_{c0} = 0.64 + 0.97(\dot{\varepsilon})^{0.091} \ . \tag{36}$$

This equation was obtained by using all three conditions from experimental data so that no "help" from analysis is needed.

The strain rate used in the calculations is taken to be the maximum of the principal rates within an element, i.e.,

$$\max(\dot{\varepsilon}_{rr}, \dot{\varepsilon}_{zz}, \dot{\varepsilon}_{\theta\theta}) \ . \tag{37}$$

The initiation of cracking within an element is based on the maximum-principal-stress criterion. In an axisymmetric (r, z, θ) geometry, the circumferential direction always provides a principal stress. The remaining two principal planes lie within the r-z plane and are given by

$$\begin{aligned} \sigma_{nn} &= \frac{\sigma_{rr} + \sigma_{zz}}{2} + \sqrt{\left(\frac{\sigma_{rr} - \sigma_{zz}}{2}\right)^2 + \sigma_{rz}^2} \ , \\ \sigma_{tt} &= \frac{\sigma_{rr} + \sigma_{zz}}{2} - \sqrt{\left(\frac{\sigma_{rr} - \sigma_{zz}}{2}\right)^2 + \sigma_{rz}^2} \ , \end{aligned} \tag{38}$$

where σ_{rr}, σ_{zz}, σ_{rz} are the radial, axial and shear stresses of the r-z plane; σ_{nn} and σ_{tt} are the stresses normal and tangential to an impending crack. When a principal stress exceeds the tensile limit, a crack is considered to be initiated. The direction of the normal to an initiated crack with respect to the r-axis is given by

$$\alpha = 1/2 \arctan [2\sigma_{rz}/(\sigma_{rr} - \sigma_{zz})] . \quad (39)$$

Once a crack has been initiated, its direction is kept as a permanent record so that the stress or strain normal or tangent to the crack can be monitored during subsequent time steps. The normal, tangential, and shear strains (ϵ_{nn}, ϵ_{tt}, γ_{nt}) with respect to the crack are,

$$\begin{Bmatrix} \epsilon_{nn} \\ \epsilon_{tt} \\ \gamma_{nt} \end{Bmatrix} = \begin{bmatrix} \cos^2\alpha & \sin^2\alpha & 1/2 \sin 2\alpha \\ \sin^2\alpha & \cos^2\alpha & -1/2 \sin 2\alpha \\ -\sin 2\alpha & \sin 2\alpha & \cos 2\alpha \end{bmatrix} \begin{Bmatrix} \epsilon_{rr} \\ \epsilon_{zz} \\ \gamma_{rz} \end{Bmatrix} , \quad (40)$$

where ϵ_{rr}, ϵ_{zz}, γ_{rz} are the engineering (small) normal strains in the radial, axial directions, and shear angle in the r-z plane, respectively.

The strains of Eq. (38) within a given element are related to the stresses as follows:

$$\begin{Bmatrix} \sigma_{nn} \\ \sigma_{tt} \\ \sigma_{nt} \\ \sigma_{\theta\theta} \end{Bmatrix} = E_1 \begin{bmatrix} 1 & \nu_1 & 0 & \nu_1 \\ \nu_1 & 1 & 0 & \nu_1 \\ 0 & 0 & G/E_1 & 0 \\ \nu_1 & \nu_1 & 0 & 1 \end{bmatrix} \begin{Bmatrix} \epsilon_{nn} \\ \epsilon_{tt} \\ \gamma_{nt} \\ \epsilon_{\theta\theta} \end{Bmatrix} , \quad (41)$$

where $\nu_1 = \nu/(1 - \nu)$, $E_1 = 2G(1 - \nu)/(1 - 2\nu)$, E is Young's modulus of elasticity, ν is Poisson's ratio, and G is the shear modulus.

Equation (41) is also used for the case where cracking is assumed to have initiated, but a definite crack opening is not as yet present. Such a state is assumed to be possible in the presence of microcracks in brittle materials [16]. For purposes of illustrating the crack initiation model, the principal stresses of Eq. (41) are arranged so that $\sigma_1 > \sigma_2 > \sigma_3$. Initially σ_1 will be equal to σ_{nn} or $\sigma_{\theta\theta}$ depending on which one is of greater magnitude. Since cracking is based on the maximum principal stress, crack initiation should

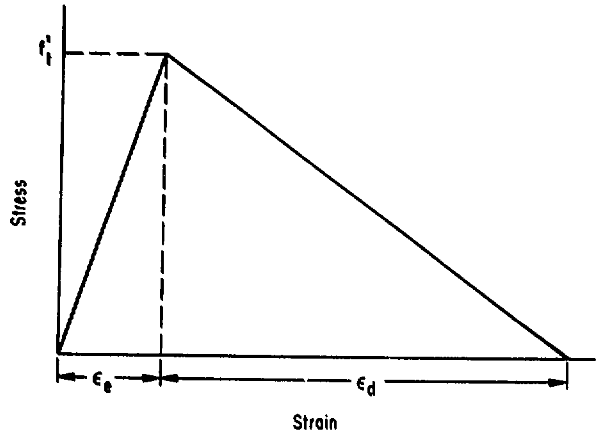

Fig. 4. Stress-Strain Model of Cracking Material Under Transient Conditions.

first occur normal to σ_1. Once the principal stress σ_1 reaches or exceeds the tensile limit f_t', the stress normal to the impending crack is prescribed and is usually independent of the strain normal to the crack. At the instant when the maximum uniaxial tensile limit is reached or exceeded by the principal stress, the stress normal to the impending crack is set equal to the tensile limit f_t'. During the subsequent time increments, the tensile stress normal to the impending crack is reduced to zero linearly over a prescribed characteristic strain ϵ_d in Fig. 4:

$$\sigma_1 = f_t'\left(1 - \frac{\varepsilon - \varepsilon_e}{\varepsilon_d}\right) ; \qquad \varepsilon_e < \varepsilon < (\varepsilon_e + \varepsilon_d) , \tag{42}$$

where ϵ_d is the normal strain, extending from initiation of cracking to crack opening, and ϵ_e is the strain corresponding to the tensile limit f_t', shown in Fig. 4. This equation applies for the range of normal strains shown; if $\varepsilon > (\varepsilon_e + \varepsilon_d)$, then the formation of a crack is considered completed; a fully developed crack is assumed to have occurred.

It should be noted that if any of the principal stresses are prescribed, the other principal stresses are affected correspondingly. For example, if the prescribed stress across the crack is taken to be σ_A, the strain component ϵ_{nn} in Eq. (41) is solved for and substituted into the expressions of the other principal stresses. The state of stress in the element becomes:

$$
\left.\begin{aligned}
\sigma_1^* &= \sigma_A , \\
\sigma_2^* &= \sigma_2 + \nu_1(\sigma_A - \sigma_1) , \\
\sigma_3^* &= \sigma_3 + \nu_1(\sigma_A - \sigma_1) , \\
\sigma_{nt}^* &= G\gamma_{nt} .
\end{aligned}\right\} \quad (43)
$$

Similarly, if two principal stresses σ_A, σ_B are prescribed, the element state of stress becomes:

$$
\left.\begin{aligned}
\sigma_1^* &= \sigma_A , \\
\sigma_2^* &= \sigma_B , \\
\sigma_3^* &= E\varepsilon_3 + \nu(\sigma_A + \sigma_B) , \\
\sigma_{nt}^* &= G\gamma_{nt} ,
\end{aligned}\right\} \quad (44)
$$

where ε_3 is the minimum principal strain. Finally, if all three principal stresses are prescribed, σ_A, σ_B, σ_C, then the state of stress becomes:

$$
\left.\begin{aligned}
\sigma_1^* &= \sigma_A , \\
\sigma_2^* &= \sigma_B , \\
\sigma_3^* &= \sigma_C , \\
\sigma_{nt}^* &= G\gamma_{nt} .
\end{aligned}\right\} \quad (45)
$$

Note that the prescribed stresses σ_A, σ_B, σ_C need not be equal. This may occur, for example, if a second or third crack forms in an element. As long as no fully developed cracks exist, concurrent crack development is assumed to originate in orthogonal directions.

It may be noted that a more realistic way to model progressive tensile cracking would be to take into account the nonlinearity of tensile stress-strain behavior and tensile strain-softening, which would entail a nonlinear tensile stress-strain relationship. This relationship must exhibit the elastic anisotropy introduced by partial cracking in particular directions. To express this in a tensorially invariant form, it would be necessary to postulate a damage tensor whose components describe the reduction of elastic stiffness in various directions.

The transformation of principal stresses to stresses in cylindrical coordinates (r, z, θ) must also be provided for. Since θ is the principal coordinate, no change is necessary for the circumferential stress $\sigma_{\theta\theta}$. The stress components in the r-z plane, however, require the following transformation

$$\begin{Bmatrix} \sigma_{rr} \\ \sigma_{zz} \\ \sigma_{rz} \end{Bmatrix} = \begin{bmatrix} \cos^2\alpha & \sin^2\alpha & -\sin2\alpha \\ \sin^2\alpha & \cos^2\alpha & \sin2\alpha \\ 1/2\sin2\alpha & -1/2\sin2\alpha & \cos2\alpha \end{bmatrix} \begin{Bmatrix} \sigma^*_{nn} \\ \sigma^*_{tt} \\ \sigma^*_{nt} \end{Bmatrix} . \tag{46}$$

The state of stress in an element with one fully developed radial crack is established by the previous equations provided that $\sigma_{\theta\theta}$ is set to zero. However, with a fully developed crack in the r-z plane the presence of aggregate interlock makes the conditions somewhat more complicated. It has been suggested [17] that the effect of aggregate interlock can be accounted for by a shear reduction term as follows:

$$\begin{Bmatrix} \sigma_{tt} \\ \sigma_{nt} \\ \sigma_{\theta\theta} \end{Bmatrix} = \frac{E}{1 - \nu^2} \begin{bmatrix} 1 & 0 & \nu \\ 0 & \frac{\beta(1 - \nu)}{2} & 0 \\ \nu & 0 & 1 \end{bmatrix} \begin{Bmatrix} \varepsilon_{tt} \\ \gamma_{nt} \\ \varepsilon_{\theta\theta} \end{Bmatrix} , \tag{47}$$

where β is the shear reduction factor, a constant usually taken as 0.5. This means that the shear strain tangent to the crack is assumed to be reduced by the factor β from what it would be in the absence of a crack. Although a constant factor for any crack size and aggregate surface is a rather rough estimate, it seems to yield fairly good results under static conditions.

Lacking any better means of accounting for aggregate interlock, the same approach is retained in this formulation.

Because of the existence of the shear stress due to aggregate interlock, the perpendicular to the normal of the existing crack within an element is not a principal direction. The second principal stress in the r-z plane, which is used to check for secondary cracks, and the angle of its normal with respect to the r-axis are:

$$\left.\begin{aligned} \sigma^*_{tt} &= 1/2\,\sigma_{tt} + \sqrt{(1/2\,\sigma_{tt})^2 + \sigma^2_{nt}} \,, \\ \alpha^* &= \alpha + 1/2 \arctan\left(-2\sigma_{nt}/\sigma_{tt}\right) . \end{aligned}\right\} \qquad (48)$$

The non-orthogonal cracking in the r-z plane causes another complication. With one crack fully developed and another impending, there are a total of four stress values to be prescribed but the stress tensor has only three independent components. This difficulty is resolved in the following manner: The normal stresses across the two cracks are given by Eq. (42) and the shear stress σ_{nt} of the first crack is computed by the shear reduction factor β, as described before. The shear stress σ^*_{nt} along the impending crack, however, is obtained from equilibrium considerations, as shown in Fig. 5. Note also the definition of α and α^* in Fig. 5. Moment equilibrium shows that the shear stresses tangent to the new crack is given by

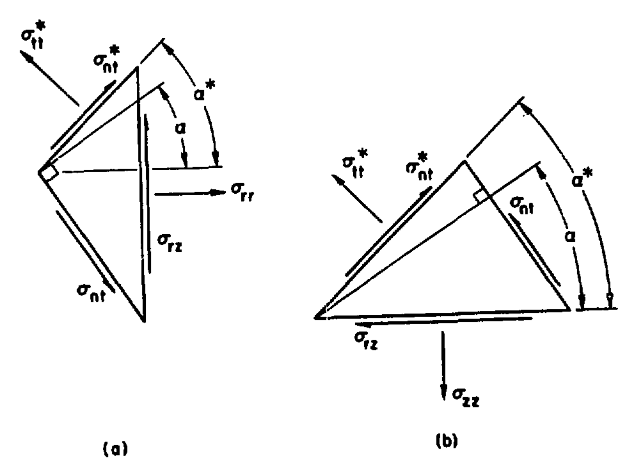

Fig. 5. Element with Two Non-Perpendicular Cracks.

$$\sigma^*_{nt} = \sigma_{nt} + \sigma^*_{tt} \tan\left(\alpha^* - \alpha\right) . \qquad (49)$$

From force equilibrium the following expressions are obtained:

$$\begin{Bmatrix} \sigma_{rr} \\ \sigma_{zz} \\ \sigma_{rz} \end{Bmatrix} = \frac{a}{\cos^2(\alpha - \alpha^*)} \begin{bmatrix} \sin\alpha \sin(2\alpha^*-\alpha) & -2\sin\alpha \cos\alpha^* \cos(\alpha-\alpha^*) \\ \cos\alpha \cos(2\alpha^*-\alpha) & 2\sin\alpha \cos\alpha^* \cos(\alpha-\alpha^*) \\ -1/2\sin2\alpha^* & 1/2(\cos2\alpha^*+\cos2\alpha) \end{bmatrix} \begin{Bmatrix} \sigma^*_{tt} \\ \sigma^*_{nt} \end{Bmatrix}. \quad (50)$$

It may be observed that Eq. (50) reduces to Eq. (46) provided that σ_{nn} is set to zero and α^* is set equal to α. Equation (50) pertains to the case where the second crack in the r-z plane is in the process of formation, or has been fully developed. Thus $\sigma^*_{tt} = f'_t$, if the second crack is at the instant of being formed, $\sigma^*_{tt} = \sigma_1$ [see Eq. (42)] during crack formation, and $\sigma^*_{tt} = 0$ if the crack is fully formed.

After the second crack in the r-z plane has fully developed and σ^*_{tt} is set to zero, the remaining stresses are calculated by

$$\begin{Bmatrix} \sigma_{nt} \\ \sigma_{\theta\theta} \end{Bmatrix} = E \begin{bmatrix} \beta G/E & 0 \\ 0 & 1 \end{bmatrix} \begin{Bmatrix} \gamma_{nt} \\ \epsilon_{\theta\theta} \end{Bmatrix}. \quad (51)$$

On the other hand, if the radial crack is postulated to have fully formed first, then $\sigma_{\theta\theta}$ is set to zero and the remaining stresses become

$$\begin{Bmatrix} \sigma_{tt} \\ \sigma_{nt} \end{Bmatrix} = E \begin{bmatrix} 1 & 0 \\ 0 & \beta G/E \end{bmatrix} \begin{Bmatrix} \epsilon_{tt} \\ \gamma_{nt} \end{Bmatrix}. \quad (52)$$

Here again, the principal stress is not σ_{tt}, but is expressed by Eq. (48) with the corresponding position. The resolution of stresses into the components of the r-z plane is accomplished by Eq. (46) where σ^*_{nn} is set to zero.

Equations (51) and (52) also apply to the case where a third crack has initiated and is in the process of formation. Then the last principal stress is assigned by Eq. (42). If all three cracks have been fully developed in the element, all stress components are due to the contribution of shear strain γ_{nt}.

Due to the oscillatory nature of the motion of the vessel, the cracking model must account for the possibility that a fully developed crack may close or an impending crack may be arrested if the strain rate changes sign. The strain normal to each crack monitors this condition: if the strain normal to a given crack is found to be less than zero, then a fully developed crack is assumed to have closed or the development of a crack is assumed to be interrupted. The element is then able to sustain compressive loading across the crack. With the closing of a crack or arrest of cracking, the tensile limit normal to the crack is changed and stored for later use. If a fully developed crack closes, then the tensile limit is set to zero. However, in case the crack formation is interrupted, the stored tensile limit is assigned that particular value of stress which corresponds to the time of crack arrest. The element is hence governed by the reduced tensile limit if and when it is again reloaded in tension.

As for the inelastic behavior in compression, only the simplest possible model consisting of a maximum compressive limit on the principal stresses, is considered at this stage. In compression the stress in the element may be defined by the previous expressions, depending on how many principal stresses reach the compressive limit f_c' at the same time. At the present, the maximum uniaxial stress f_c' is used as the maximum stress that the element may be able to sustain.

B. Reinforcement

In this analytical model, the reinforcement is superimposed over the concrete element as if it were uniformly distributed over the entire element as an anisotropic material. Uniaxial reinforcement within the element can be prescribed as a percentage of reinforcement in three directions - one being the circumferential direction, and the other two positioned arbitrarily within the r-z plane, as shown in Fig. 6.

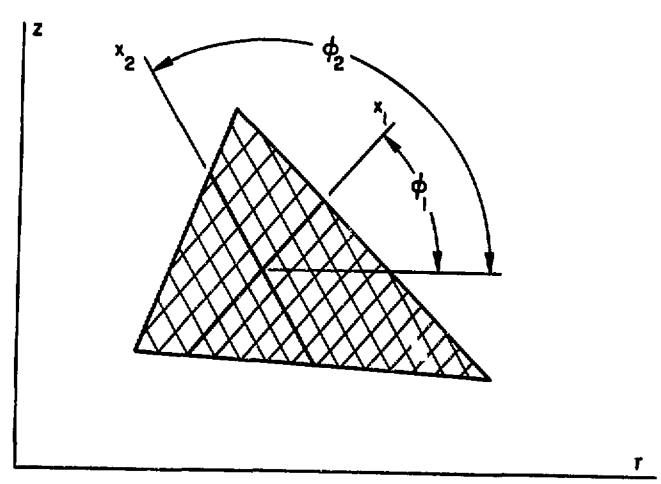

Fig. 6. Reinforcing Within Element.

For purposes of computing the stresses in the reinforcement in the r-z plane, the strain in the direction of the reinforcement must be found. If the angle between the r-axis and the axes of the reinforcement are ϕ_1 or ϕ_2, the strain along the respective directions corresponds to ε_{nn} in Eq. (41). The response of reinforcement is determined by an elastic-plastic material model. This model uses isotropic unloading.

A conventional yield value correction for mild steel is incorporated for reinforcement, i.e.,

$$(\sigma_y)_{dyn} = (\sigma_y)_{stat}\left[1 + \left(\frac{\dot{\varepsilon}}{40.4}\right)^{0.2}\right], \tag{53}$$

which accounts for the strain rate effects.

The contribution of the reinforcement stress to the total element stress is then given by

$$\sigma_T = \sigma_s A_r / A_c \,, \tag{54}$$

where A_r and A_c are the cross-sectional areas of reinforcement and concrete normal to the directions of the reinforcement. The stress in Eq. (54) needs to be transformed into the cartesian components if reinforcement lies in the r-z plane; for circumferential reinforcement, σ_T corresponds to $\sigma_{\theta\theta}$. Finally, the cartesian stress components due to concrete and steel are summed to obtain the overall stress in the element.

C. Artificial Viscosity

In the integration of the finite-element equations of motion with small time steps, such as is generally the case in explicit integration, high-frequency oscillations which are called "spurious oscillations" will appear in an undamped system. The severity of these oscillations tends to increase if the mesh is rather heterogeneous. These oscillations can be reduced and sometimes eliminated by the use of a suitable artificial viscosity, which is really a numerical damping.

An artificial viscosity of the following form is used

$$s_{ij}^{vis} = \mu\rho c\sqrt{A}\,\dot{e}_{ij} , \qquad (55)$$

$$s_{ij} = \sigma_{ij} - 1/3\ \sigma_{\ell\ell}\delta_{ij} ,$$
$$e_{ij} = \epsilon_{ij} - 1/3\ \epsilon_{\ell\ell}\delta_{ij} , \qquad (56)$$

where σ_{ij} and ϵ_{ij} are the stress and strain tensors, while s_{ij} and e_{ij} are the deviatoric stress and strain tensors, respectively, μ is approximately the fraction of critical damping.

V. COMPARISON OF ANALYSIS WITH TEST DATA

The comparison of analytical results with test data is important in validating the analytical model. This is especially true in this case because the analytical behavior of concrete under transient conditions is not yet well understood. Here we need basic experimental data for guiding the analytical formulation. This has been a difficult task because even test data of relatively simple structures under transient loading are sparse. Only some of the comparison made will be described in this report.

A. Static Test

The experimental data used in this comparison pertains to an internally pressurized, prestressed cylindrical container tested at the University of Illinois, Urbana [18]. This container simulates the containment of a nuclear reactor, and is shown in Fig. 7. The right side of Fig. 7 identifies the components of the test structure, while the left side shows the analytical model used in the comparison. As can be observed, no reinforcement is provided in the model.

The concrete is characterized by a tensile limit of 3.10 MN/m^2, a compressive limit of -49.23 MN/m^2 with an initial elastic modulus of 29.7 GN/m^2 and a Poisson's ratio of 0.15. The prestress material has a modulus of 192 GN/m^2 and a yield stress of 1655 MN/m^2. Before the internal pressurization is applied, each layer of tendons is prestressed longitudinally to a

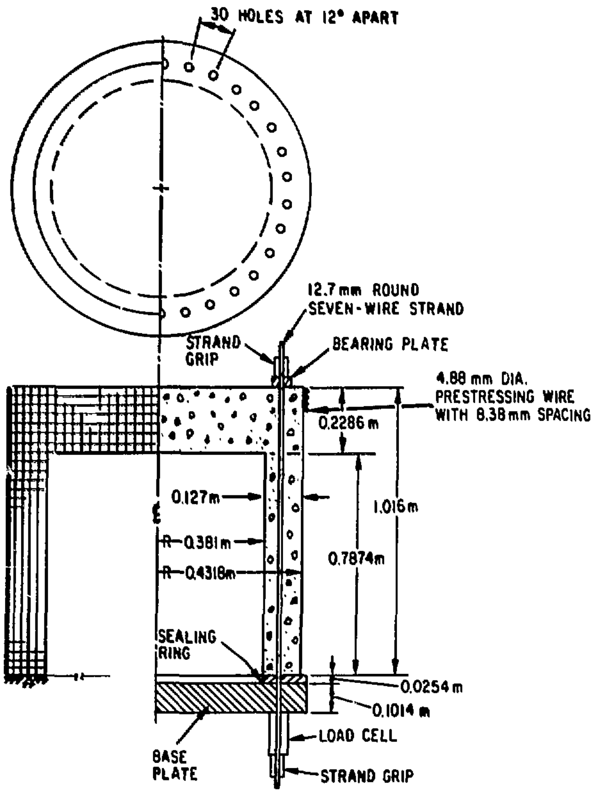

Fig. 7. Details of the Cylindrical Test Vessel.

force of 0.112 MN and prestressed circumferentially to an equivalent pressure of 3.52 MN/m^2.

It should be emphasized that while the experimental data pertains to static conditions, the analytical results are based on a computer code which is expressly written for dynamic problems. The use of a dynamic code for a static simulation is inefficient and rather expensive, but it nevertheless provides a good validation of the method for predicting static problems. It should be noted that this problem was run before dynamic relaxation was introduced into the code. With the dynamic relaxation now available, the solution of static problems should be easier. However, the accuracy of the solution in the presence of concrete cracking should be independent of the algorithm.

The static results were thus simulated by a set of individual dynamic runs, all of which involved the same prestress. The pressurization in each of these runs consisted of a ramp loading to a given pressure, followed by a constant pressure at that level. Each individual run involved a different pressure level. In the first phase, the pressurization proceeded at a loading rate higher than that encountered in the experiment.

The general response of the model would roughly follow the history of the pressurization coupled with the dynamic oscillation superimposed over the static value. The static equivalent response was thus estimated by visual elimination of the dynamic component from the overall results.

The analytical simulation of a static experiment by means of a dynamic code, as used in this comparison involves certain error sources. Because of the dynamic overshoot, the analytical model would be exposed to higher stresses, resulting in additional cracks, which in turn would make the material "softer". Thus, because of the overshoot beyond the tensile limit, the model may overestimate the true results.

Figure 8 shows the central deformation of the cover with respect to internal pressure. The close agreement is encouraging since the nonlinearity of the deflection stems from the cracking in the concrete; without cracking, the deflection would be linear along the initial slope.

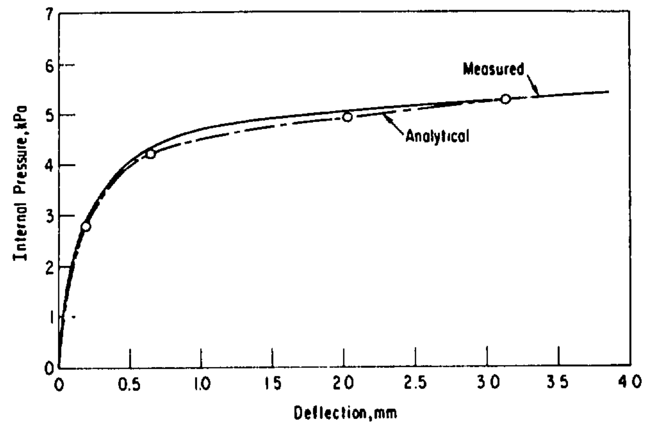

Fig. 8. Central Deflection of the Top Slab.

Figures 9 through 11 show the comparison of experimental strain readings on the cover with code calculations. Figure 9 shows the radial strain on the top surface of the cover at three radial locations. Four sets of experimental data are shown at each of the radial distances. The calculated strain falls within the experimental data.

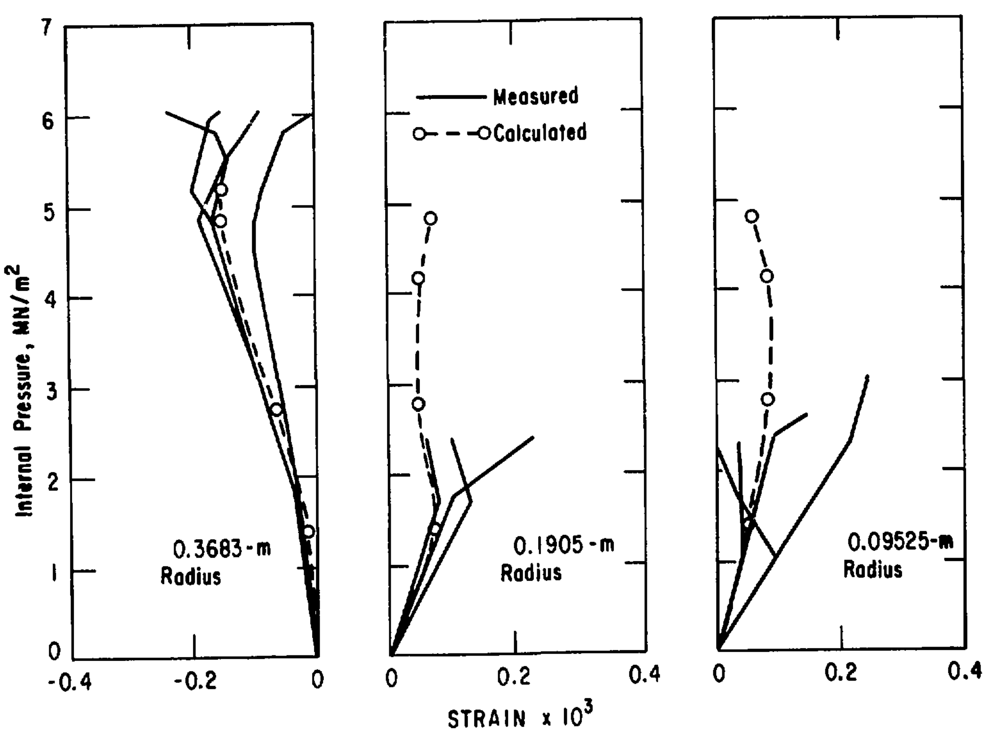

Fig. 9. Radial Strain at Top of Slab.

The radial strain at the bottom of the cover is shown in Fig. 10. Again, the data of four gauges, each located at the same distance from the center, is compared with the calculated results. The calculated values compare quite well with the measurements.

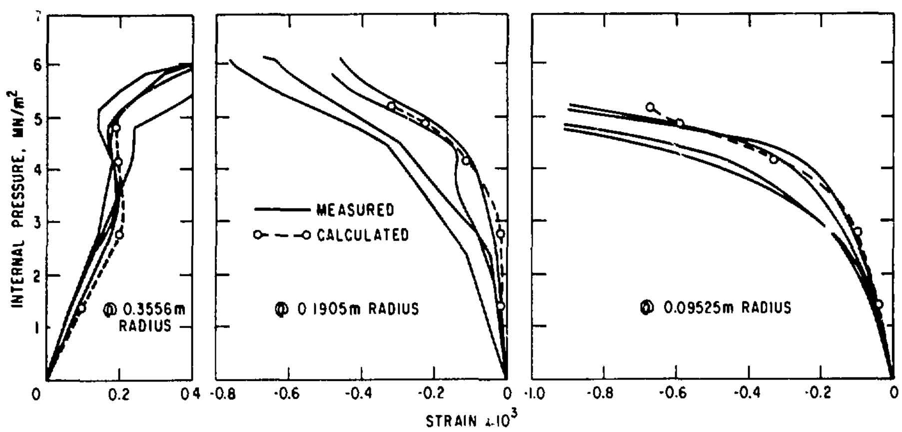

Fig. 10. Radial Strain at Bottom of Slab.

The circumferental strains at the bottom of the cover are given in Fig. 11. The calculated results show a stiffer response at the low pressures. This is consistent with the elastic representation of the concrete in compression; in reality, concrete exhibits softening with increasing compression. This effect seems to be offset at higher pressures by the occurrence of cracking.

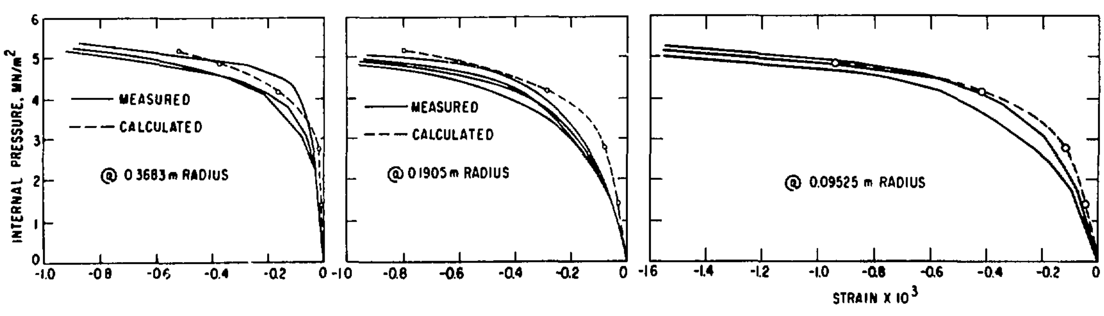

Fig. 11. Circumferential Strain at Bottom of Slab.

The overall agreement between experiment and calculation is surprisingly good. All the results shown pertain to the cover of the model. Since the cover is not reinforced, the quality of comparisons largely reflect on the crack modeling of concrete. A comparison of experiment and analysis under dynamic conditions will be presented in subsequent sections.

B. Dynamic Tests

In our comparisons of analytical results with experimental data, we have concluded that concrete cracking is greatly dependent on the strain rate of loading; much better correlation between experiment and analysis could be obtained when the cracking limit was made dependent on the strain rate. Because available data is insufficient, we have introduced an extrapolation for taking the strain rate effects into account. However, this procedure requires other test data from which the needed information could be inferred. The first illustration of this section thus deals with the "calibration" where a tensile limit and strain rate relationship is obtained.

1. Tension-Reinforced Beam

Rather simple test specimens involving substantial cracking are beams tested at the University of Illinois, Urbana [19]. The beam tested is shown in Fig. 12 where the right-hand side shows the characteristics of the beam and the left-hand side shows the analytical model.

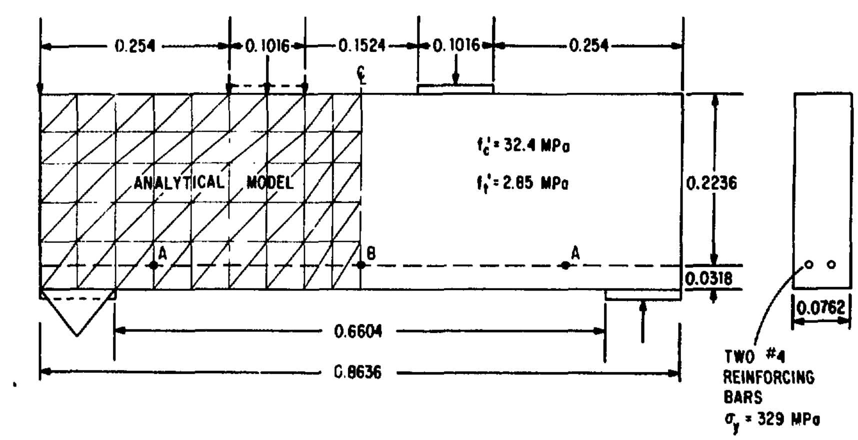

Fig. 12. Details of the Concrete Test Beam and the Analytical Model.

Figure 13 shows the history of the applied load and Fig. 14 the history of the central deflection. Figure 14 gives two sets of experimental results, together with the analytical deflection. The analytical results represent the best fit with the experimental data. The important points to match here were the maximum deflection and the permanent set. Strain history

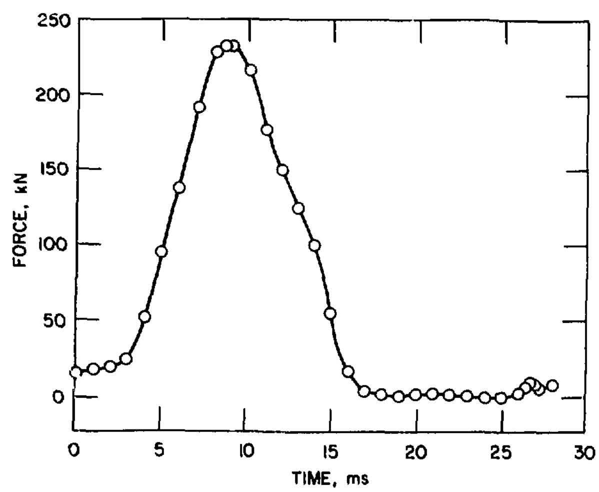

Fig. 13. History of the Applied Force.

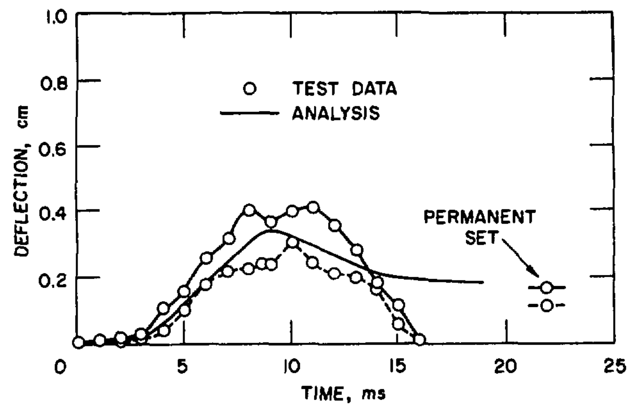

Fig. 14. Central Deflection of the Beam.

of the reinforcing steel is shown in Fig. 15, which refers to location A in Fig. 12. Two sets of experimental values exist which pertain to points which should have equal response because of symmetry. The analytical strain reported here is the average strain for two adjoining horizontal elements.

Figure 16 shows additional experimental strain results for the identical locations, but for the second reinforcing rod. The analytical strain results shown in Fig. 15 are reproduced in Fig. 16 for comparison.

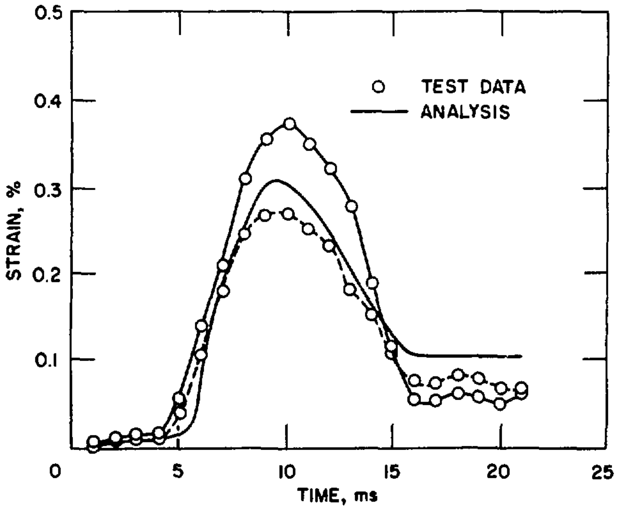

Fig. 15. Strain History of Reinforcing Steel at Location A.

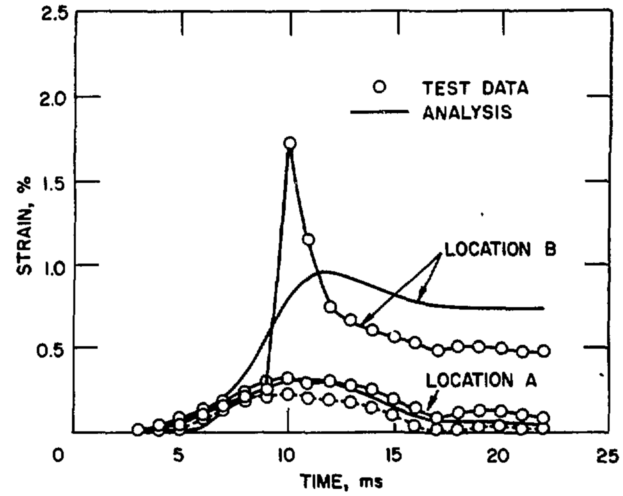

Fig. 16. Strain History of Steel at Locations A and B.

The steel strains on the centerline of the beam are also shown in Fig. 16. The analytical results indicate a final permanent set of 0.76%, whereas the experimental value is ~ 0.5%. The analytical results given in the figures pertain to the following values of the constants in Eq. (35):

$$a = 0.94, \quad b = 3.79, \quad c = 0.37,$$

and the strain rate correction of reinforcing steel for yield stress given in Eq. (53). These values were found by trial and error to best compare with experimental data. These constants depend to some extent on other variables, not only of the analytical model, but also on the characteristics of the concrete constitutive model, discretization of the analytical model, the artificial viscous damping, etc. With the large number of variables involved, the question arises as to how well the analytical model calibrated for the strain rate in this experiment predicts results in other structures. The extension of this analytical model to other test structures will be reported in subsequent sections.

2. Long Test Beam

The experimental data referred to in this section originated also at the University of Illinois, Urbana [20]. The details of the reinforced concrete beam tested together with the supporting system, are shown in Fig. 17(a), while the analytical model used in the comparison is given in Fig. 17(b). Figure 18 indicates the time-history of the applied load on the beam.

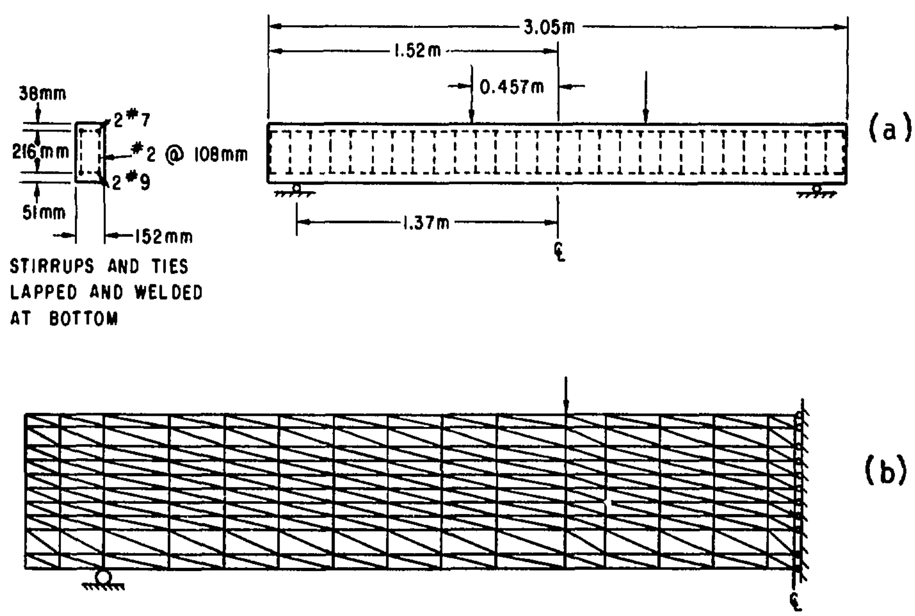

Fig. 17. Dimensions of the Test Beam (a) and Corresponding Model (b).

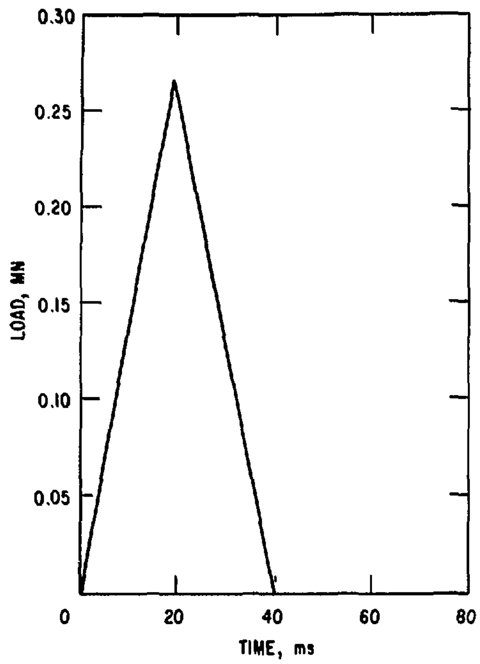

Fig. 18. Idealized Input Load Acting on the Beam.

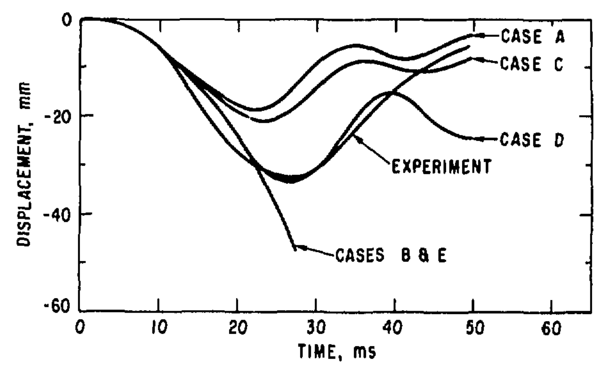

Fig. 19. Vertical Displacement History at the Center of the Beam.

Since the reinforcement is assumed to be distributed evenly throughout each of the elements, it may be characterized by averaged vertical and horizontal reinforcement densities in the interior elements. The only elements without reinforcement are located within the top and bottom layers of the beam.

The time history of the central deflection of the beam is shown in Fig. 19, which depicts the experimental data and a number of results pertaining to analytical predicitons. For Case A, the strain rate relationship derived in the previous section was used. The maximum analytical beam displacement is 55% lower than that of the experiment. It appears that the rate dependence of the cracking limit makes the analytical model too stiff in this case. The sensitivity of the analytical model to other parameters was then investigated in order to establish the source of the discrepancy.

First, strain rate dependence on the limit of concrete cracking was ignored in the model which is denoted as Case B in Fig. 19. Very large displacements were predicted and excessive cracking prevented numerical completion of the solution. Next we assumed the same static properties for concrete, but permitted only one crack per element. This corresponds to Case C in Fig. 19.

Since the model tested possesses considerable reinforcing, as compared to the model described in the previous section, we chose to investigate the reinforcing steel properties. Case D corresponds to the analytical results where the rate dependence on the yield stress of reinforcing steel was neglected and cracking was limited to one crack per element. This curve comes closest to the experimental results. On the other extreme, cracking was not limited but strain rate effects for reinforcement were neglected and the results of beam displacement are shown as Case E.

The parameter study shows that the strain-rate effects of concrete play a small role here. However, the strain rate effects of the reinforcing steel are of importance. This illustration shows that "calibration" of analytical model is not a simple matter and must involve considerable thought. An independent calibration of one variable is meaningful only if the effect of the other variables is insignificant.

3. Simple PCRV Model

The third set of results given here is for the PCRV model tested at Foulness [21] for the British fast reactor safety program. A cross-section of this cylindrical PCRV model is shown in Fig. 20. The model was loaded through charges submerged in the pool of water. The explosive used was the same PETN/polystyrene foam as in the COVA [22] test for which a well-defined equation of state exists. The experimental pressure records were not spatially consistent, so, in order to obtain a set of consistent pressure records for use of the PCRV analysis, an ICECO [23] simulation of the charge detonation and subsequent pool swell and slug impact was made. In the ICECO analysis, the behavior of the charge was described by the equation of state derived for the COVA experiments [22]:

$$p = Ae^{-9V} + Be^{-2.4V} + C^{-1.1} ,$$

where A = 17.039 GPa, B = 1.1595 GPa, C = 53.56 MPa, and V is the specific volume. The equation of state for water is of the form

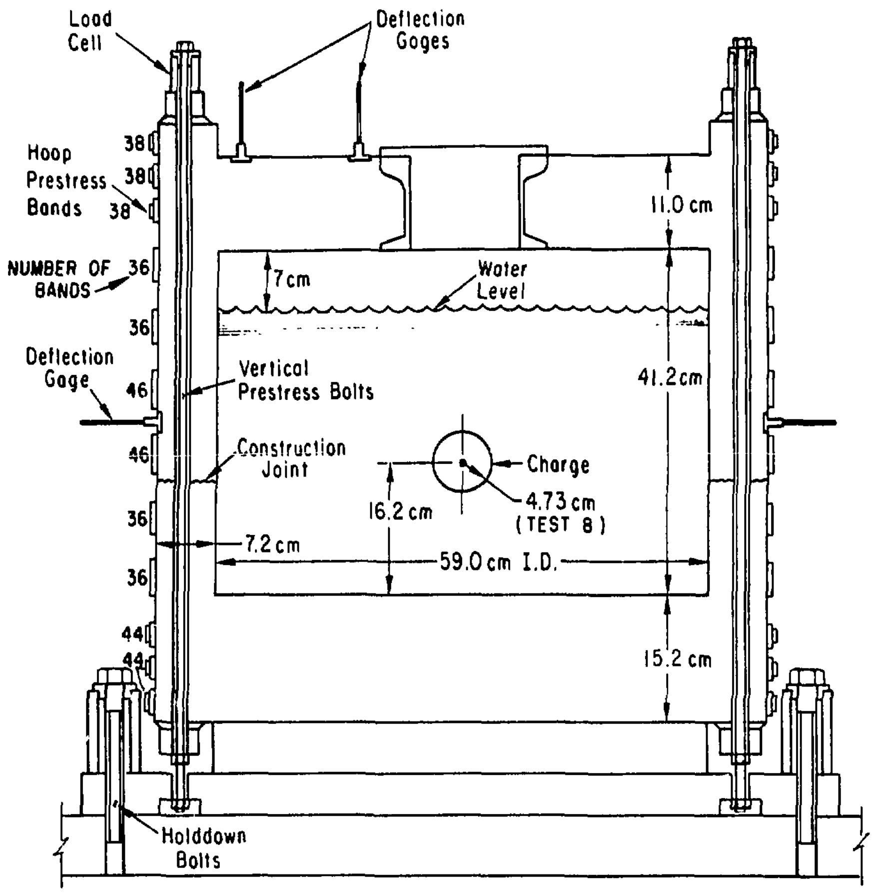

Fig. 20. Geometry of Test Model.

$$p = \frac{B_0}{B_0'}\left[\left(\frac{V_0}{V}\right)^{B_0'} - 1\right],$$

where B_0 = 1.9895 GPa, B_0' = 6.985, and V_0 is the initial specific volume. The air above the surface of the water was allowed to escape during the excursion and to present no resistance to compression. The pressure histories on the walls of the PCRV were stored and used to load the prestressed PCRV analytical model.

The PCRV model is shown in Fig. 21. Axisymmetric linear-displacement triangular elements with one integration point per element were used. Four layers of elements were used in the cylindrical walls, and although this is barely sufficient for an accurate simulation of the bending, the primary response is in a hoop mode, for which this discretization is more than adequate. The stable time step for this model was 2 μs. Material properties of the model are given in Table I.

The prestressing tendons were modelled by rod elements placed as shown in Fig. 21. An elastic-plastic material model with isotropic strain hardening was used for the rods. These elements were connected to the concrete elements through sliding interfaces, so that the prestressing force was applied to the PCRV only at the anchors of the tendons.

In the PCRV model the vertical tendons consisted of 18 high strength bolts of 12.7 mm diameter which were prestressed to an initial tension of 49 kN.

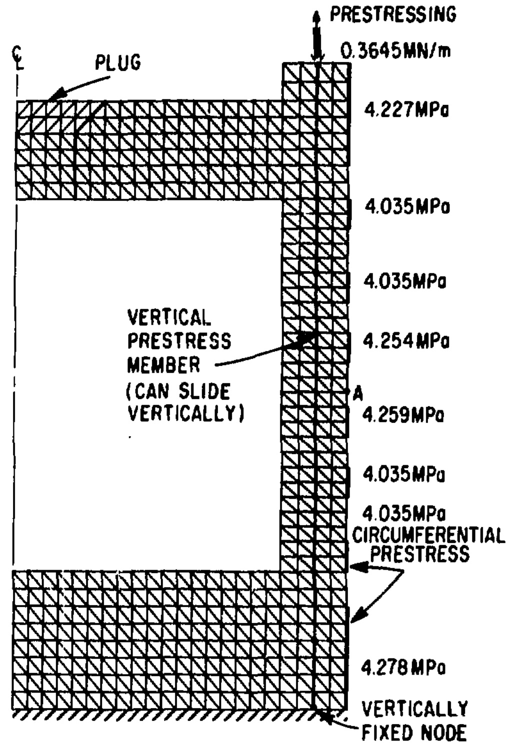

Fig. 21. The PCRV Analytical Model.

Hoop prestress was applied by winding on the model 18 gauge (1.22 mm) diameter high tensile wire at a tension of 1.46 kN. Due to the relaxation of the model, the estimated prestress in the tests were as follows [24]:

1. Hoop tendon loads were reduced 70% to 65% of their failure strength, and

2. Vertical tendon loads were reduced from 74% to 64% of their failure strength.

These estimated prestress conditions were used in our simulations; the equivalent values are indicated in Fig. 21.

The prestressing operation was simulated by applying equal and opposite forces to the concrete and prestressing members at the anchors with the tendons. A static solution was obtained for this condition by the dynamic relaxation procedure [25]. During the dynamic relaxation procedure, no cracking was allowed in the concrete to prevent spurious cracking from dynamic overshoots. The results of this solution then served as initial conditions for the transient solutions.

Table I. Material Properties.

Properties of Concrete	
Density	2400 kg/m^3
Modulus of elasticity	44000 MPa
Stress-strain data (yield)	Tensile failure 5 MPa Compressive failure strength 65 MPa
Poisson's ratio	0.17
Properties of Prestress Steel	
Density	8000 kg/m^3
Initial modulus of elasticity	200000 MPa
Tensile and compressive limits	Hoop prestress: 18 gage wire (1.22 mm dia.) Tensile failure 2085 N
	Vertical prestress: 17.7 mm bolt Tensile yield load 66030 N Tensile failure load 78680 N
Poisson's ratio	0.30

Before the analytical simulation of the experimental data is described, we will briefly review the salient features of the Foulness test data. This data pertains to a series of dynamic loadings on a single PCRV model. The explosives used in the tests were small at the start and were increased in size until failure of the vessel occurred. Some of the available data are given in Table II.

Table II. Maximum Radial Displacement at the Side Wall.

Test No.	Charge, g	Pressure[b], MPa	Displacement, mm	
			Experiment	Analysis
1 & 2	2.5	3.6 & 2.5	-	0.103
3 & 4	14 & 12	6.8 & 15.9	-	0.343
5	27	19.8	1.0, 0.77	0.871
6	54	25.5	1.27	1.54
7	112	44.0	Failure	

[b] Recorded peak pressure on the side wall.

The use of the same vessel in the whole series of tests confronted us with the dilemma of whether or not to maintain the cracks from previous simulations. We found that the concrete model described here overestimates damage, so that if the cracks are maintained through the entire series of simulations, complete failure is predicted at a lower load than observed experimentally. Therefore, we performed these analyses with either an undamaged initial state or at most precracking from one previous analysis.

Displacement time histories at the midpoint of the cylindrical vessel were only available for tests 5 and 6. Figure 22 shows the experimental data of test 5 along with a purely elastic simulation and a simulation without precracking. An attempt to account for precracking is demonstrated in Fig. 23, where only the precracking from the loading of test 4 is included. The individual cases shown in Fig. 23 pertain to different strain-rate relationships of tensile cracking assumed and are shown in Fig. 24. The same strain dependence of the tensile cracking limit is used during loading of both test 4 and test 5.

The computer simulations with cracking replicate the principal features of the experiment: the period of the displacement is increased, and the amplitude is increased as compared to the elastic solution. The precracked simulation is more accurate in the period, while that without precracking is more accurate in the maximum amplitude. Both solutions exhibit the absence of any permanent displacement found in the experiment: the prestressing tendons remain elastic and close the cracks after the load is released. It is of interest that the solutions with and without precracking bound the observed maximum displacement.

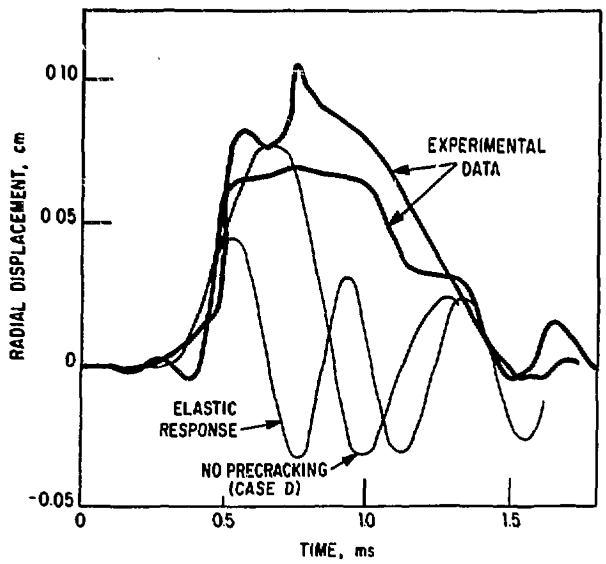

Fig. 22. Comparison of Side-Wall Displacement with Analysis for Test 5.

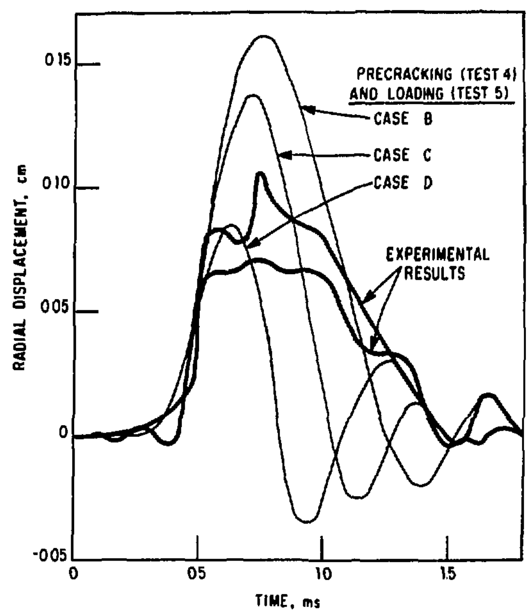

Fig. 23. Consideration of Precracking for Test 5.

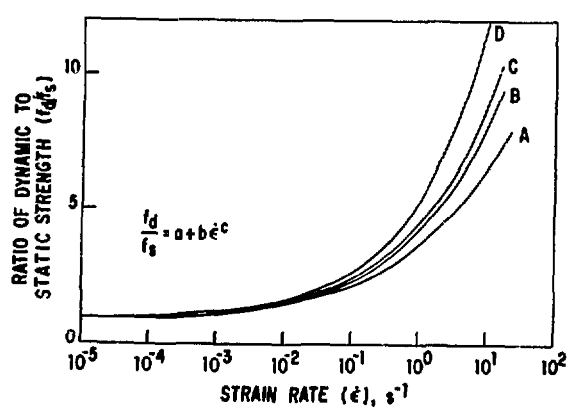

Fig. 24. Assumed Cracking Limit Dependence of Concrete.

The deformation history for test 6 is given in Fig. 25 where test data are compared to two analytical solutions. The analytical results consist of a purely elastic solution and another with cracking where precracking had not been taken into account. The correlation between the analytical predictions and experiment is almost identical to test 5: the amplitude agrees quite well, but the solution without precracking no longer bounds the observed displacement from below.

In Ref. [21] it was conjectured that a proper inclusion of the added mass of the fluid would improve the correlation between experiment and analysis. However, it turns out that added mass is quite small and changes the results by at most 5%.

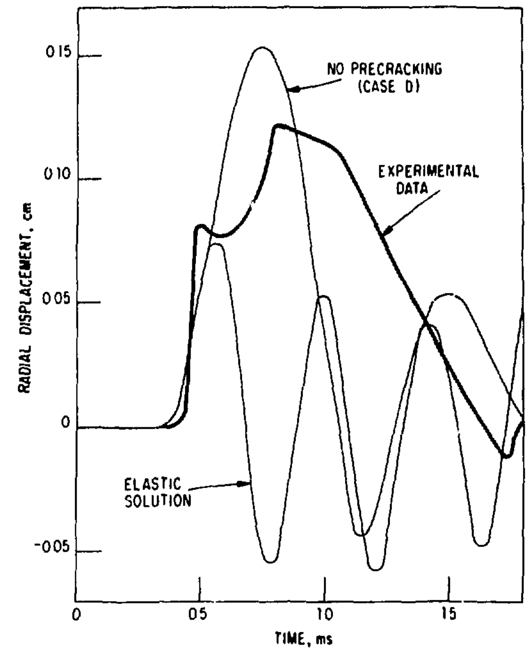

Fig. 25. Comparison of Side-Wall Displacement with Analysis for Test 6.

VI. CONCLUSIONS

The results presented in this report reflect the current capability of the DYNAPCON code to treat dynamically loaded PCRV structures. The comparisons of experiment and code results shows reasonable agreement for many features of available experiments, but also some shortcomings. The calculations correctly predict the magnitudes of the displacements for tests 5 and 6 of the Foulness model tests. In addition, displacement time histories obtained from the calculation reproduce the salient features of the experimental records: period elongation and amplitude increase as compared to an elastic solution, and the absence of permanent displacement. However, the period still underestimates the experiment, while the amplitude is generally somewhat large. In test 5, the solutions with and without precracking bound the observed record.

One parameter in the transient modeling of concrete, which was introduced in this investigation, is the effect of strain rate on the tensile strength limit of concrete. The relevance of this parameter, although inferred initially from intuition and numerical considerations and later observed in other brittle materials [15], appears to be quite important in modeling of concrete cracking. Experimental evidence is necessary to resolve this issue. Once an experimental determination of the rate-dependence can be ascertained than the remaining questions of crack modeling can be addressed.

Although it is quite clear that analytical modeling of concrete cracking must include strain-rate effects, it is also evident that this is not the only cause for the discrepancies between computations and experiments. This is substantiated by the observation that analytical simulations could not quite match the experimental shapes of the deflections. Either the amplitude or the period of response could be varied by changing different variables, yet both of them could not be matched with experiment for the same run.

The need for experimental evidence into the phenomenology of concrete cracking cannot be overemphasized. Closer agreement with experimental data will eventually require better analytical modeling of the actual cracking phenomenon.

ACKNOWLEDGEMENTS

The experimental data used in this paper was provided to ANL by Mr. W. B. Dale, Fast Reactor Development, United Kingdom Atomic Energy Authority. Mr. J. N. Bradbury of Nuclear Power Company (Risley) Limited provided additional information on the prestress relaxation of the test model. The actual testing was conducted at Foulness, where Mr. V. C. Pickett was the principal investigator.

The help of Dr. T. Belytschko in constructing the analytical model is gratefully acknowledged. The author acknowledges the council of Dr. S. H. Fistedis who formulated the concept of PCRV for primary containment and initiated the work of this concept. Appreciation is extended to the individual members of the Engineering Mechanics Program, especially Dr. R. Kulak, for valued suggestions during the course of this study.

This work is part of the Engineering Mechanics Program of the Reactor Analysis and Safety Division, Argonne National Laboratory and is supported by the U.S Department of Energy.

REFERENCES

1. A. Nilson, "Nonlinear Analysis of Reinforced Concrete by the Finite Element Method," Proc. ACI Journal 65(g) (September, 1968).

2. J. H. Argyris, G. Faust, and K. J. Willam, "Limit Load Analysis of Thick-Walled Concrete Structures - A Finite Element Approach to Fracture," Comp. Meth. Appl. Mech. and Eng. 8, pp. 215-243 (1976).

3. J. R. H. Otter, "Dynamic Relaxation Compared with Other Iterative Finite Difference Methods," Nucl. Eng. Design 3, pp. 183-185 (1966).

4. J. A. Holland, "Dynamic Relaxation Applied to Local Effects," Conf. on PCRVs, Inst. Civ. Eng. pp. 587-595 (1968).

5. A. C. Cassell and R. E. Hobbs, "Numerical Stability of Dynamic Relaxation Analysis of Nonlinear Structures," Int. J. for Num. Meth. in Eng. 10, (6), p. 1407 (1976).

6. A. H. Marchertas, et al., "Analysis and Application of Prestressed Concrete Reactor Vessels for LMFBR Containment," Nucl. Eng. Design 49, pp. 155-173 (1978).

7. A. H. Marchertas, et al., "Extension of HCDA Safety Analysis to Large PCRV Containment Structures," Trans. 4th SMiRT Conf., Paper E 4/1, San Francisco (1977).

8. R. H. Evans and M. S. Marathe, "Microcracking and Stress Strain Curves for Concrete in Tension," Materiaux et Constructions (Materials and Structures), V. 1 #1, Jan.-Feb. 1978, p. 61-64.

9. T. B. Belytschko and B. J. Hsieh, "Nonlinear Transient Finite Element Analysis with Convected Coordinates, Int. J. Num. Methods Eng., pp. 255-272 (1973).

10. T. J. K. Hughes, et al., "Explicit-Implicit-Finite Elements," FENOMECH Conf. Stuttgart, 1978.

11. V. V. Novozhilov, "The Theory of Thin Elastic Shells," GRONINGEN: P. Nordhoff (1959).

12. A. M. Neville, "Properties of Concrete," 2nd Edition, J. Wiley & Sons, New York (1973).

13. D. McHenry and J. J. Shideler, "Review of Data on Effect of Speed in Mechanical Testing of Concrete," ASTM Sp. Tech. Publ. No. 185, 72 (1956).

14. D. J. McNeeley and S. D. Lash, "Tensile Strength of Concrete," J. Amer. Concs. Inst. 60 (751) (1963).

15. D. E. Grady and M. E. Kipp, "Oil Shale Fracture and Fragmentation at Higher Rates of Loading," paper presented at the 20th U.S. Symp. on Rock Mechanics, Austin, Texas (June 4-6, 1979).

16. L. Seaman, et al., "Calculational Models for Ductile and Brittle Fracture," Poulter Laboratory Technical Report 003-76, SRI (June, 1976).

17. M. Suidan and W. C. Schnobrich, "Finite Element Analysis of Reinforced Concrete," J. of the Structural Div. ASCE, Vol. 99, No. ST 10, pp. 2109-2122 (October, 1973).

18. S. L. Paul, et al., "Strength and Behavior of Prestressed Concrete Vessels for Nuclear Reactors - Volume I," University of Illinois Civil Engineering Studies, Structural Research Series No. 346, Urbana (1969).

19. R. E. Untauer, "Behavior and Design of Deep Structural Members, Part 4, Dynamic Tests on Reinforced Concrete Deep Beams," Technical Report to Air Force Special Weapons Center, AFSWC TR-59-72, Part 4, (May, 1960).

20. A. Feldman, et al., "Investigation of Resistance and Behavior of Reinforced Concrete Members Subjected to Dynamic Loading, Part III," University of Illinois, Report No. DASA-1259, D74-174, Urbana, Illinois (1962).

21. A. H. Marchertas and T. B. Belytschko, "Comparison of Transient PCRV Model Test Results with Analysis," Trans. 5th Int. Conf. on SMiRT, Paper H 8/2, Berlin (1979).

22. I. G. Cameron, N. E. Hoskin,, and M. J. Lancefield, "Charge Development and Analysis of Recent UK Experiments in the COVA Model Test Programme," Trans. of the 4th Int. Conf. on SMiRT, Paper E 2/1, San Francisco (August, 1977).

23. C. Y. Wang, "ICECO - An Implicit Eulerian Method for Calculating Fluid Transients in Fast-Reactor Containment," Argonne National Laboratory Report, ANL-75-81 (December, 1975).

24. Personal communication from J. N. Bradbury, Civil Department, Nuclear Power Company (Risley) Limited, Warrington Road, Risley, Warrington, Cheshire WA3 6BZ, England.

25. A. H. Marchertas, T. B. Belytschko, and Z. P. Bazant, "Transient Analysis of LMFBR Reinforced/Prestressed Concrete Containment," Trans. 5th Int. Conf. on SMiRT, Paper H 8/1, Berlin (1979).

APPENDIX

INPUT INSTRUCTIONS TO DYNAPCON

Card Type	Columns	FORTRAN Name	Description
1			Title Card. (80A1).
	1-80	TITLE	80 alpha-numeric characters to identify the job; these characters will be printed as a heading.
2			First Parameter Card. (6I5,E10.6,I5).
	1-5	NNODE	Number of nodes in the analytical model.
	6-10	NELE	Number of elements.
	11-15	NUMMAT	Number of material types.
	16-20	NUMDIS	Number of nodes at which one or more displacement components are prescribed.
	21-25	MXSTEP	Number of time steps to be taken.
	26-30	NDGREE	Number of degrees of freedom per node (2 for this version).
	31-40	DELT	Time step Δt; if KONTRL(8) $\neq$ 0 of Card 3, then use $\Delta t = \Delta t_{min} \sqrt{\Delta t_{max} / \Delta t_{min}}$.
	41-45	NPRES	Number of load units (see Cards 11).
	46-50	NSLID	Number of sliding interface lines (see Cards 12).
3			Second Parameter Card. (16I5).
	1-5	KONTRL(1)	KONTRL(1) = 1: For axisymmetric problem. KONTRL(1) = 2: For plane stress problem. KONTRL(1) = 3: For plane strain problem.
	6-10	KONTRL(2)	KONTRL(2) = 0: No reading from or writing on auxiliary units. KONTRL(2) = 1: Write on auxiliary unit 8. KONTRL(2) = 2: Read from auxiliary unit 9. KONTRL(2) = 3: Read from auxiliary unit 9 and write on auxiliary unit 8.
	11-15	KONTRL(3)	KONTRL(3) = 0: Any nodes for which node cards are not given on Cards 7 will be equispaced. KONTRL(3) > 0: Any nodes for which node Cards 7 are not given will be spaced so that the ratio of distances between consecutive nodes are KONTRL(3)/100.

Card Type	Columns	FORTRAN Name	Description
3 (cont'd)			
	16-20	KONTRL(4)	KONTRL(4) = 0: For pressure-time loading. KONTRL(4) ≠ 0: For impulse (initial velocity) loading.
	21-25	KONTRL(5)	Percent of critical (stiffness-proportional) artificial damping.
	26-30	KONTRL(6)	Percent of critical (mass-proportional) artificial damping.
	31-35	KONTRL(7)	Circular frequency of the structure to be specified with KONTRL(6).
	36-40	KONTRL(8)	KONTRL(8) = 0: Dynamic relaxation is not used. KONTRL(8) > 0: Dynamic relaxation is to be used, where KONTRL(8) = $\Delta t_{max}/\Delta t_{min}$ - 1 in the element mesh.
	41-45	KONTRL(9)	KONTRL(9) = 0: Input loading not derived from auxiliary units. KONTRL(9) > 0: Input loading derived from auxiliary unit 4 and acting on elements 1 (one) through KONTRL(9) during the course of the solution.
	46-50	KONTRL(10)	Total number of fully cracked elements allowed in the solution; after reaching KONTRL(10) number of fully cracked elements the solution terminates.
	51-55	ICRACK	ICRACK = 0: No concrete elements used in the analytical model. ICRACK = 1: Concrete elements are used in the analytical model.

Note: Cards 4 and 5 are used only if ICRACK = 1 (see Card 3).

Card Type	Columns	FORTRAN Name	Description
4			Concrete Parameters. (6F10.0,2I10).
	1-10	RASYTI	RASYTI = 0: Minimum printing of concrete cracking (only fully cracked elements are indicated). RASYTI = 1: Detailed initiation and completion of cracking within the concrete elements is indicted.

Card Type	Columns	FORTRAN Name	Description
4 (cont'd)			
	11-20	PR	Poisson's ratio of concrete.
	21-30	BETA	Degree of full shear to be retained in the concrete elements (usually BETA = 0.5).
	31-40	ERB	Elastic modulus of reinforcing steel.
	41-50	SYIELD	Yield stress of reinforcing steel.
	51-60	DKCOEFF	Magnitude of strain from initiation to completion of cracking.
	61-70	NR	Number of straight-line portions of the stress-strain diagram of reinforcing steel.
5			Stress-Strain Data for Reinforcing Steel. (8E10.0)
	1-10	EE(1)	First strain. } Coordinates of first point
	11-20	EE(2)	First stress. } Coordinates of first point
	21-30	EE(3)	Second strain. } Coordinates of second point.
	31-40	EE(4)	Second stress. } Coordinates of second point.
	⋮		
	61-70	EE(7)	Fourth strain. } Coordinates of fourth point.
	71-80	EE(8)	Fourth stress. } Coordinates of fourth point.

Note: (1) Use another card if needed to describe the piece-wise linear stress-strain diagram.

(2) If KONTRL(2) < 2 (see Card 2) then two sets of cards (Cards 2 through 5) must be used. This is usually a continuation run. In addition, one or two extra cards must be supplied as follows:

Card Type	Columns	FORTRAN Name	Description
5a			(11I5).
	1-5	ICOUNT	Number of cracked elements to be input.

Note: Cards 5b are used only if ICOUNT > 0.

Card Type	Columns	FORTRAN Name	Description
5 (cont')			
5b			Crack Information (I5,5X,6E10.4).
	1-5	LD	Number of cracked element.
	11-20	STR9	Index of circumferential crack.
	21-30	STR8	Index of first crack in the r-z (or x-y) plane.
	31-40	STR7	Index of second crack in the r-z (or x-y) plane.
	41-50	STR6	Angle of first crack measured from r (or x) axis.
	51-60	STR5	Angle of second crack measured from r (or x) axis.
	61-70	SMC	Secant modulus for unloading.

Note The information on Card 5b can be (and usually is) generated by punching cards during the preceding part of several runs (see NCRK on Card 10a).

Card Type	Columns	FORTRAN Name	Description
6			Material Properties for Flexural Beam or Shell Elements.
6a			(2I5).
	1-5	MTYPE	Material type number.
	6-10	NTYPE	NTYPE = 1: For beam or shell elements.
6b			(6E10.4).
	1-10	E(1,MTYPE)	Mass density.
	11-20	E(2,MTYPE)	Young's modulus.
	21-30	E(3,MTYPE)	Yield stress.
	31-40	E(4,MTYPE)	Plastic modulus (second slope of the stress-strain curve).
	41-50	E(5,MTYPE)	Space reserved for width of beam (not used in this version).

Card Type	Columns	FORTRAN Name	Description
6b (cont'd)			
	51-60	E(6,MTYPE)	Ultimate stress.
6c			(6E10.4)
	1-10	E(7,MTYPE)	Poisson's ratio.
	11-20	E(8,MTYPE)	Height of beam or shell (needed only if not specified in dummy node data on Card 7).
6			Material (other than Concrete) Properties for Plane and Axisymmetric Elements.
6a			(2I5)
	1-5	MTYPE	Material type number.
	6-10	NTYPE	NTYPE = 2: For continuum elements.
6b			(6E10.4)
	1-10	E(1,MTYPE)	Density.
	11-20	E(2,MTYPE)	Young's modulus.
	21-30	E(3,MTYPE)	Yield stress.
	31-40	E(4,MTYPE)	Plastic modulus.
	41-50	E(5,MTYPE)	E(5,MTYPE) = 0: For solid elements; bulk modulus if element is used to simulate fluid. If element is fluid then E(2,MTYPE) and E(6,MTYPE) should be zero.
	51-60	E(6,MTYPE)	Ultimate stress.
6c			(6E10.4).
	1-10	E(7,MTYPE)	Poisson's ratio.
	11-20	E(8,MTYPE)	E(8,MTYPE) = 0: For no artificial damping. E(8,MTYPE) = 1: For use with artificial damping.

Card Type	Columns	FORTRAN Name	Description
6c (cont'd)			
	21-30	E(9,MTYPE)	Linear damping coefficient for hydrostatic stresses.
	31-40	E(10,MTYPE)	Linear damping constant for deviatoric stresses.
6			Material Properties for Reinforced Concrete Elements.
6a			(2I5).
	1-5	MTYPE	Material type number.
	6-10	NTYPE	NTYPE = 4: For continuum concrete elements.
6b			(6E10.4).
	1-10	E(1,MTYPE)	Density of concrete.
	11-20	E(2,MTYPE)	Concrete compressive limit.
	21-30	E(3,MTYPE)	Initial elastic modulus.
	31-40	E(4,MTYPE)	Concrete tensile limit.
	41-50	E(5,MTYPE)	Area ratio of reinforcement in r (or x) direction.
	51-60	E(6,MTYPE)	Area ratio of reinforcement in z (or y) direction.
6c			(6E10.4).
	1-10	E(7,MTYPE)	Area ratio of reinforcement in circumferential direction.
	11-20	E(8,MTYPE)	E(8,MTYPE) = 0: For no artificial damping. E(8,MTYPE) = 1: For artificial damping to be used.
	21-30	E(9,MTYPE)	Linear damping coefficient for hydrostatic stresses.
	31-40	E(10,MTYPE)	Linear damping constant for deviatoric stresses.

Card Type	Columns	FORTRAN Name	Description
7			Nodal Coordinates. (I5,5X,2E10.4).
	1-5	N	Node number.
	6-20	XC(N)	r (or x) coordinate for real nodes; for "dummy" nodes this could specify the height of the beam or shell.
	21-30	YC(N)	z (or y) coordinate of node N.

Note: Coordinates for nodes equispaced between two nodes will be automatically generated if the data cards for intermediate nodes are skipped.

Card Type	Columns	FORTRAN Name	Description
8			Element-Node Relationship. (10I5).
	1-5	M	Element number.
	6-10	NODE(1,M)	Node N1 of element M.
	11-15	NODE(2,M)	Node N2 of element M.
	16-20	NODE(3,M)	Node N3 of element M.
	21-25	NODE(4,M)	Node N4 of element M.
	26-30	NODE(5,M)	NODE(5,M) = 0: If KONTRL(8) = 0. NODE(5,M) ≠ 0: If KONTRL(8) ≠ 0, the element M is a prestress element and it is connected to only one continuum element.
	31-35	NODE(6,M)	NODE(6,M) = 0: For solid elements. NODE(6,M) ≠ 0: For elements simulating fluid.
	41-45	NODE(8,M)	NODE(8,M) = 1: For axisymmetric elements. NODE(8,M) = 2: For plane stress elements. NODE(8,M) = 3: For plane strain elements. NODE(8,M) = 8: For concrete elements.
	46-50	MTYP	Material number for element M.
	51-55	NTYP	NTYP = 1: For flexural element. NTYP = 2: For triangular continuum element. NTYP = 3: For triangular fluid element.

Note: (1) For triangular element N3 = N4 and the nodes must be numbered clockwise.
(2) For flexural elements N3 and N4 are "dummy" nodes and are associated with nodal rotations.

Card Type	Columns	FORTRAN Name	Description
8 (cont'd)			

Note: (3) Node cards for elements which can be generated by adding one to all node numbers of the previous element need not be included; the node data for these elements will be generated automatically. The card associated with the last element is required.

(4) For axisymmetric configurations the meridional prestress elements should use NODE(8,M) = 2.

Card Type	Columns	FORTRAN Name	Description
9			Prescribed Nodal Displacements. (I10,E10.4).
	1-7	N	Node at which one or more displacement components are prescribed to be zero.
	8	I	I = 0: For unconstrained displacement of the $\bar{r}$ (or $\bar{x}$) component. I = 1: For zero displacement of the $\bar{r}$ (or $\bar{x}$) component.
	9	J	J = 0: For unconstrained displacement $\bar{z}$ (or $\bar{y}$) component. J = 1: For zero displacement of the $\bar{z}$ (or $\bar{y}$) component.
	11-20	ANGLE	Angle of inclination of the boundary coordinate axis $\bar{r}$ (or $\bar{x}$) relative to the global r (or x) axis measured counterclockwise in degrees.

Note: The rotational degree of freedom is controlled by I for the dummy nodes; I = 0 for unconstrained rotation and I = 1 for zero rotation.

Card Type	Columns	FORTRAN Name	Description
10			Output Control.
10a			(5I10).
	1-10	NPFREQ	Output frequency; time history records of specified nodal and element information will be printed every NPFREQ time step.
	11-20	NPRU	Number of nodal-related time history records: displacements, velocities, accelerations, forces, etc.
	21-30	NPRS	Number of element-related time history records: stresses, strains, internal forces, etc.

Card Type	Columns	FORTRAN Name	Description
10a (cont'd)			
	31-40	NPIC	Number of complete output records at specified time steps; this may consist of all nodal and element records at the given time step.
	41-50	NCRK	NCRK = 0: No information on cracking requested. NCRK = 1: Final cracking information to be printed at the end of the solution. NCRK = 2: Final information to be printed and punched on cards in the same format as given for Cards 5b.
10b			NPRU Specifications. (8I10).
	1-7		Node number for which a specified nodal record is to be printed.
	8	J	J = 1: For r (or x) component or the rotation for dummy nodes. J = 2: For z (or y) component.
	9	K	K = 0: For displacement. K = 1: For velocity. K = 2: For acceleration. K = 3: For external force. K = 4: For internal force.
	10	L	L = 0: If no plotting required. L = 1: For nodal time history to be plotted on printer. L = 2: For nodal time history to be plotted on printer and auxiliary unit such as Calcomp.
10c			NPRS Specifications for Continuum Elements. (8I10).
	1-7		Element number for which information is to be printed.
	8-9	M	M = 1: Strain $\hat{\varepsilon}_r$ (or $\hat{\varepsilon}_x$). M = 2: Strain $\hat{\varepsilon}_z$ (or $\hat{\varepsilon}_y$). M = 3: Engineering shear strain $\hat{\gamma}_{rz}$ (or $\hat{\gamma}_{xy}$). M = 4: Hoop strain $\hat{\varepsilon}_{\theta\theta}$ (for axisymmetric case).

Card Type	Columns	FORTRAN Name	Description
10c (cont'd)			
	8-9 (cont'd)	M	M = 5: Stress $\hat{\sigma}_r$ (or $\hat{\sigma}_x$). M = 6: Stress $\hat{\sigma}_z$ (or $\hat{\sigma}_y$). M = 7: Shear stress $\hat{\sigma}_{rz}$ (or $\hat{\sigma}_{xy}$). M = 8: Hoop stress $\hat{\sigma}_{\theta\theta}$ (for axisymmetric case).
	10	L	L = 0: For no printing requested. L = 1: For information to be plotted on printer. L = 2: For information to be plotted on printer and on auxiliary unit such as Calcomp.
10c			NPRS Specifications for Flexural Elements. (8I10).
	1-7		Element number for which information is desired.
	8-9	M	Index given in the following table, where the circumscribed numbers refer to integration points throuh the depth of the beam or shell.

Station	①	②	③	④	⑤	⑥	⑦	⑧	⑨	⑩
$\hat{\varepsilon}_x$	1	2	3	4	5	6	7	8	9	10
$\hat{\sigma}_x$	11	12	13	14	15	16	17	18	19	20
$\hat{\varepsilon}_\theta$	21	22	23	24	25	26	27	28	29	30
$\hat{\sigma}_\theta$	31	32	33	34	35	36	37	38	39	40
yield pt	41	42	43	44	45	46	47	48	49	50

Card Type	Columns	FORTRAN Name	Description
10c (cont'd)			

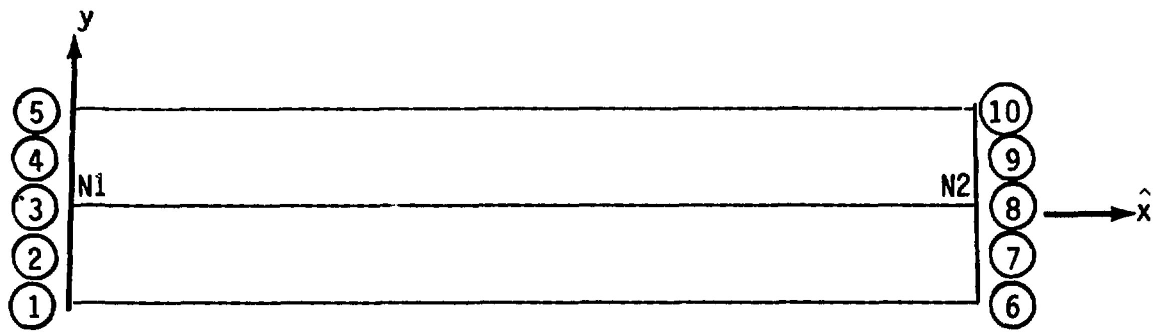

	10	L	L = 0: For no printing. L = 1: For information to be plotted on printer. L = 2: For information to be plotted on printer and on auxiliary unit such as Calcomp.
10d			NPIC Specification. (2I10).
	1-10		Time step at which a complete output as specified by KONT is desired.
	11-20	KONT	KONT = 1: Displacements at all nodes. KONT = 2: Displacements and current coordinates at all nodes. KONT = 3: Displacements, coordinates, velocities and accelerations at all nodes. KONT = 4: Displacements, coordinates, velocities, accelerations, of all modes, strains and stresses of all elements.
11			Loading Specifications.
11a			(5I5).
	1-5	I	Load unit number.
	6-10	NDNOD	Number of nodes associated with the load unit.

Card Type	Columns	FORTRAN Name	Description
11a (cont'd)			
	11-15	IVOL(I)	IVOL(I) = 1: Pressure history is prescribed and load unit is part of axi-symmetric surface. IVOL(I) = 2: Pressure history is prescribed and load unit is part of plane surface. IVOL(I) = 8: For circumferential prestress load unit. IVOL(I) = 9: For meridional prestress load unit; in this case NDNOD = 3.
	16-20	INT1	Interval, spacing between nodes on load unit for automatic load unit generation; if INT1 > 0, the load unit is generated by adding INT1 to the previous node number starting with the node specified on Card 11c.
	21-25	NPT	Number of pressure-time point pairs of a piece-wise linear curve to be specified on Cards 11b.
11b			Pressure History Input. (8E10.0).
	1-10	PT(1,I)	Time } First point on pressure-time plot.
	11-20	PT(2,I)	Pressure }
	21-30	PT(3,I)	Time } Second point on pressure-time plot.
	31-40	PT(4,I)	Pressure }
	41-50	PT(5,I)	Time } Third point on pressure-time plot.
	51-60	PT(6,I)	Pressure }
	61-70	PT(7,I)	Time } Fourth point on pressure-time plot.
	71-80	PT(8,I)	Pressure }

<u>Note</u>: Use another card to describe the pressure-time loading if needed. A total of eight pressure-time pairs can be specified for each load unit. If pressure is zero at time zero then this pair need not be input.

Card Type	Columns	FORTRAN Name	Description
11b			Inpulse Input. (8E10.0).
	1-10	PT(1,I)	Prescribed initial velocity component tangent to load unit.
	11-20	PT(2,I)	Prescribed initial velocity component normal to load unit.
	21-30	PT(3,I)	Impulse multiplication factor of the first node (use zero if the first node is not on line of symmetry, and set PT(3,I) = 2 if the first node is on the line of symmetry).
	31-40	PT(4,I)	Impulse multiplication factor of the last node [PT(4,I) = 0 if last node is not on line of symmetry, PT(4,I) = 2 if last point is on line of symmetry).
11c			Nodes Associated with the Pressure-Time Load Unit. (16I5).
	1-5	KPRES(1)	First node on load unit; if all nodes can be generated from KPRES(1) by addition of increment INT1, then only KPRES(1) need be specified.
	6-10	KPRES(2)	Second node on load unit.
	11-15	KPRES(3)	Third node on load unit.
	etc.		
11c			Nodes Associated with the Circumferential Prestress Unit. (16I5).
	1-5	KPRES(1)	First to last nodes on prestressing vessel.
	6-10	KPRES(2)	
	.	.	
	.	.	
	.	.	
		KPRES(NDNOD/2)	

Card Type	Columns	FORTRAN Name	Description
11c (cont'd)			
		KPRES(NDNOD/2+1)	First to last nodes on the prestressed surface.
	.	.	
	.	.	
	.	.	
		KPRES(NDNOD)	
11c			Nodes Associated with the Meridional Prestress Unit. (16I5).
	1-5	KPRES(1)	Node of prestress vessel where the prestressing load is applied.
	6-10	KPRES(2)	Next to the last node of the prestressed structure where sliding takes place.
	11-15	KPRES(3)	Node of the prestressed structure corresponding to the node KPRES(1).
12			Sliding Interface Cards.
12a			(16I5).
	1-5	M	Sliding interface number.
	6-10	ND1	Number of node pairs on sliding interface.
	11-15	INT1	Automatic interval generator for sliding interface nodes starting with KSLID(1,I) on Card 12b; if INT1 > 0 the node numbers of sliding interface are generated by adding INT1 to successive nodes.
	16-20	INT2	Automatic interval generator for sliding interface nodes starting with KSLID(2,I) on Card 12b.
	21-30	SLIPAR(1,M)	Static coefficient of friction.
	31-40	SLIPAR(2,M)	Dynamic coefficient of friction.

Card Type	Columns	FORTRAN Name	Description
12a (cont'd)			
	41-50	SLIPAR (3,M)	SLIPAR(3,M) = 0: For no sliding friction to be considered [then also set SLIPAR(1,M) = 0 and SLIPAR(2,M) = 0]. SLIPAR(3,M) = 1: For sliding friction to be applied.
12b			Nodes on Sliding Interface. (16I5).
	1-5	KSLID(1,I)	First pair of nodes on sliding interface.
	6-10	KSLID(2I)	
	11-15	KSLID(3,I)	Second pair of nodes on sliding interface.
	16-20	KSLID(4,I)	
		⋮	
	etc.		

<u>Note</u>: (1) Each pair of nodes on the sliding interface must initially have the same coordinates.

(2) Cards 13, 14 and 15 are intended for modifying the mass matrix in conjunction with dynamic relaxation. They are needed only if KONTRL(8) $\neq$ 0.

Card Type	Columns	FORTRAN Name	Description
13			(16I5).
	1-5	NRM	Number of nodes where the mass is to be modified; if NRM = 0 then Cards 14 and 15 are not required.
14			(16I5).
	1-5	NN(1)	Node number of first mass to be modified.
	6-10	NN(2)	Node number of second mass to be modified.
	11-15	NN(3)	Node number of third mass to be modified.
		⋮	

Card Type	Columns	FORTRAN Name	Description
		NN(NRM)	Node number of last mass to be modified.
15			Mass Multiplication Factors. (8E10.4)
	1-10	RMASS(1)	Original mass at node NN(1) will be multiplied by RMASS(1).
	11-20	RMASS(2)	Original mass at node NN(2) will be multiplied by RMASS(2).
		•	
		•	
		•	
		RMASS(NRM)	Original mass at node NN(NRM) will be multiplied by RMASS(NRM).